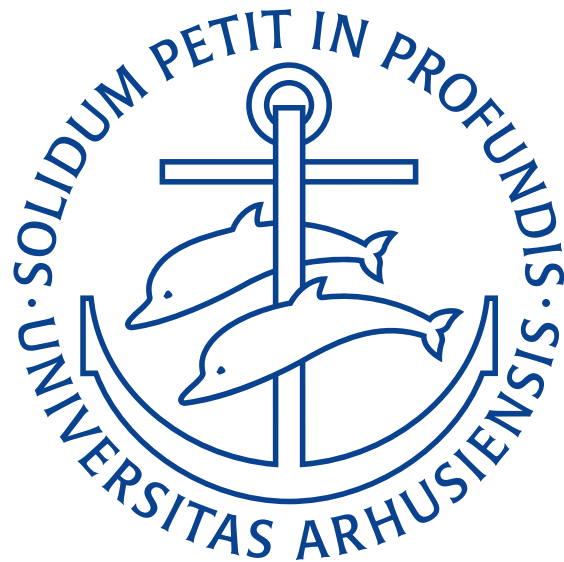MASTER'S THESIS

AN EXPERIMENTAL STUDY OF THE DECAY OF ^{21}MG

SOFIE TILBÆK NIELSEN

SUPERVISOR: KARSTEN RIISAGER

DEPARTMENT OF PHYSICS AND ASTRONOMY
AARHUS UNIVERSITY

NOVEMBER 2016

Abstract

This thesis checks the previous decay scheme [13] for β-delayed proton emission from ^{21}Mg near the proton drip-line. First, the project is motivated and previous results are briefly presented. Subsequently different types of decays are presented with emphasis on selection rules and the β-delayed particle emission which is relevant here. Next, the experiment which was carried out in April 2015 at the ISOLDE facility at CERN is described. An short description of ISOLDE is followed by a more thorough explanation of the detector setup. The energy loss of particles in matter is outlined for photons and charged particles and the latter is used for calculating energy loss in dead layers relevant for calibrations. The structure of data in ROOT format is presented and the use of the AUSAlib framework is accentuated. Next, the calibrations of silicon and germanium detectors are presented and attempts to improve the calibrations are discussed. Then, the experimental findings are presented and discussed. The preliminary proton and γ spectra are presented and line widths are interpreted. A new half-life for ^{21}Mg of 120.5(3) ms is determined from a good fit to the time distribution of the β-delayed protons. The advantages of the present detector telescope setup is discussed by presenting different spectra. The anti-coincidence spectra between front and back detector shows how to remove punch through events and a combined spectrum shows that the punch through events can be added to the spectrum to increase the energy range of the spectrum from a thin detector. A two dimensional spectrum showing the energy loss in front and back detector respectively provides a visual method for distinguishing between different types of particles. The main purpose of this study is unfolded in the γ coincidence analysis where proton spectra are constructed with gates on γ energies corresponding to γ transitions between the first excited levels in ^{20}Ne. A coincidence between a proton peak and a photon of a specific energy is confirmed if the relation $N_{p\gamma} = N_p \, \varepsilon_\gamma$ is reasonably satisfied within the uncertainties. The relative intensities are calculated based on the peak contents in the single spectra. Finally, the results are summarised in a decay scheme for ^{21}Mg and a table of relative intensities and compared to the previous results from [13]. Most of the previously assigned peaks are confirmed by the coincidence analysis. The placement of a peak from the 8135(15) keV level in ^{21}Na is disproved and a new peak from the 5020(9) keV level in ^{21}Na to the first excited state in ^{20}Ne is proposed. New relative intensities of three peaks including a peak from the IAS are proposed based on the γ coincidence analysis. In the last chapter, points for future work are suggested and the prospects of the applied setup are assessed.

Resumé (Abstract in Danish)

Formålet med dette specialeprojekt er at tjekke det tidligere henfaldsskema [13] for β-forsinket protonemission fra ^{21}Mg, der ligger tæt på protondryplinjen. Først fremstilles en motivation for projektet og tidligere resultater præsenteres kort. Dernæst beskrives eksperimentet, der ligger til grund for dette projekt. Eksperimentet blev udført på ISOLDE på CERN og derfor følger en kort beskrivelse af ISOLDE samt derefter en grundigere præsentation af detektorsetuppet. Der redegøres for energitabet for fotoner og ladede partikler i stof og dette bruges til at beregne energitab i dødlag på detektorerne, hvilket er vigtigt for at kunne lave præcise kalibreringer. Data præsenteres i aktuelle ROOT-format og brugen af værktøjerne fra AUSAlib-biblioteket er understreget. Derefter følger en redegørelse for kalibreringerne af silicium- og germaniumdetektorerne samt en diskussion af forsøg på forbedringer heraf. Herefter kommer en præsentation og vurdering af de eksperimentelle resultater. De første plots af proton- og fotonspektre presenteres med et lille fokus på linjebredder. En ny halveringstid for ^{21}Mg på 120.5(3) ms bestemmes ud fra et godt fit til tidsfordelingen af de β-forsinkede protoner. Fordelene ved teleskopkonfigurationen af siliciumdetektorerne i setuppet synliggøres ved hjælp af forskellige typer af spektre. Spektret med antikoincidens mellem front- og bagdetektor viser virkningen af at fjerne protoner, der ellers ville trænge hele vejen igennem frontdetektoren, fra spektret. Et kombineret spektrum viser, hvordan de gennemtrængende protoner, der stopper i bagtælleren, kan føjes til spektret fra frontælleren for at udvide energiskalaen i spektret. Et todimensionelt plot, der viser energitabet i front- og bagdetektor mod hinanden, giver en visuel metode til at adskille forskellige typer af partikler. Hovedformålet med dette specialeprojekt nås med γ-koincidensanalysen, hvor protonspektre konstrueres kun med protoner, der er detekteret i samme udlæsning som en foton med en bestemt energi. Disse fotonenergier svarer til fotonovergange mellem de laveste eksiterede niveauer i ^{20}Ne. Koincidensen mellem en protonpeak og en fotonovergang er bekræftet, hvis relationen $N_{p\gamma} = N_p \, \varepsilon_\gamma$ vurderes opfyldt inden for usikkerheden. Relative intensiteter beregnes ud fra indholdet af peaks i enkeltprotonspektrene. Slutteligt sammenfattes resultaterne i et henfaldsskema for ^{21}Mg og en tabel over relative intensiteter, hvorefter de sammenholdes med tidligere resultater fra [13]. De fleste af de peaks, der indgik i det tidligere henfaldsskema er bekræftede med koincidensanalysen. Placeringen af en peak fra 8135(15) keV-niveauet i ^{21}Na er tilbagevist mens en ny peak, der går fra 5020(9) keV-niveauet i ^{21}Na til den første eksiterede tilstand i ^{20}Ne er foreslået. Nye relative intensiteter for tre peaks inklusiv en peak fra den isobare

analoge tilstand i ^{21}Na er frestillet baseret på koincidensanalysen. I det sidste kapitel foreslås punkter, hvor analysen kunne forbedres eller bekræftes, og perspektiverne i det anvendte setup vurderes.

CONTENTS

INTRODUCTION

The main aim of nuclear physics is to study the structure and dynamics of the atomic nucleus. Depending on the size of the nucleus and its location in the periodic table it exhibits different characteristics. Far from the valley of stability in the nuclear chart lies increasingly unstable nuclei with possible exotic decay modes. Investigation of these drip-line nuclei has been of great interest during the last decades as the improvement of equipment has expanded opportunities within research. Hence, for example, the nuclear research group at Aarhus University has improved their studies of ^{31}Ar over three generations of projects due to gradual improvements in the ability to produce pure sources with sufficient intensity and evolution of detection methods (see eg. [7] and [11]). The lesson to learn from these previous drip-line nuclei studies is that with technological development there is often something new to see and interpret even within previously well-understood nuclei.

With these potential advances in mind we turn to investigations of ^{21}Mg. ^{21}Mg β decays to ^{21}Na and has several β-delayed proton emission branches to different levels in ^{20}Ne;

$$
\begin{aligned}
^{21}_{12}\text{Mg} \ \to \ &^{21}_{11}\text{Na} + e^+ + \nu_e \\
&\hookrightarrow {}^{20}_{10}\text{Ne}^{(*)} + p \\
&\quad \hookrightarrow {}^{20}_{10}\text{Ne} + \gamma \ ,
\end{aligned} \tag{1.1}
$$
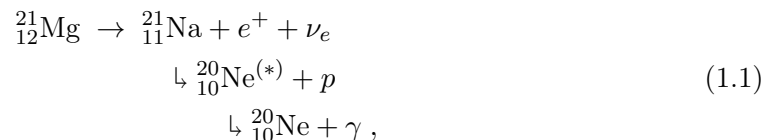
This study seeks to shed light on this β-delayed proton emission and thereby gain new information as well as consolidate previous results on this isotope on the proton drip-line.

In November 2011 Morten V. Lund et al. [14] carried out an experiment which studied β-delayed proton emission from ^{21}Mg. That study consisted in interpreting spectra like the one in figure 1.1 and the resulting decay scheme regarding β-delayed proton emission from that study is shown in figure 1.2. The results are presented in [13] and [14]. As the present study seeks to check these previous results for the β-delayed proton branches and thus refers back to them, the p_x notation from figure 1.1 is adopted. The previous study [13] and [14] showed a substantial improvement in statistics compared to earlier studies and this resulted in the discovery of some new β-delayed proton emission branches and an improvement of the precision in general - and thus all studies of ^{21}Mg that predate [13] are now outdated. A reliable placing of the β-delayed proton branches in a decay scheme relies upon considerations about the β decay of ^{21}Mg, analysis of the resulting proton spectra
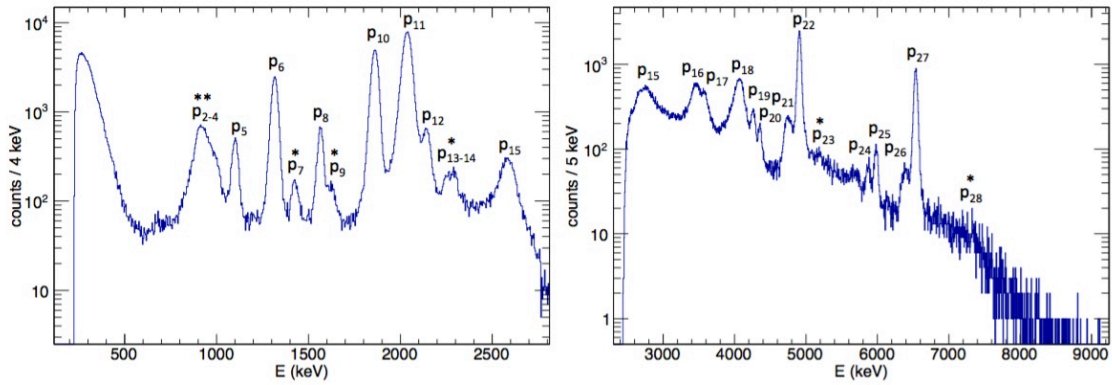
Figure 1.1: Proton single spectrum from the previous study by Morten V. Lund [13] which shows the numbering of peaks which is adopted in the present study.
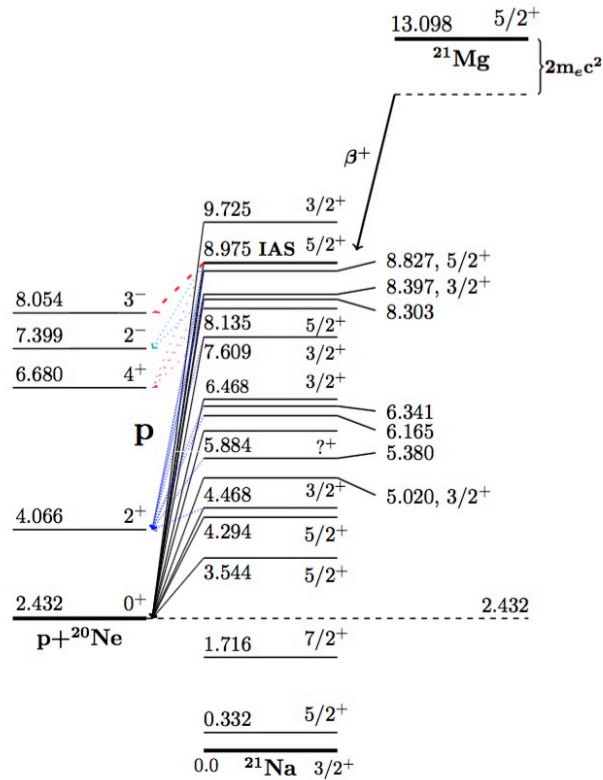

Figure 1.2: Decay scheme from the study by Morten v. Lund et al.[14] on data from the November 2011 experiment.

and preferably a study of possible subsequent photon emissions from excited levels in ^{20}Ne. The setup for the November 2011 experiment was limited as it did not include photon detectors. The results of the November 2011 experiment contradicts earlier results and thus - though the results seem reliable - a test of the results with data from an experimental setup including photon detectors is preferred. This is exactly the aim of the present study.

In April 2015 Morten V. Lund et al. [15] carried out an experiment investigating the β-delayed proton emission from ^{20}Mg and in connection to this obtained extensive measurements on ^{21}Mg for calibration purposes. This data provides the opportunity to also investigate the the decay of ^{21}Mg with a setup including photon detectors. The main purpose of the present thesis is thus to obtain a clearer picture of the enhanced decay scheme proposed in [14] and [13] through application of a more complex coincidence analysis of the April 2015 data involving γ-rays.

Being good and driven researchers we do not want to miss the chance of making the most of the ^{21}Mg data even though the original purpose was just to make good calibrations. When the data is obtained one is almost obliged to present the possible results in order to drive the research forward and contribute to the overall poll of knowledge.

AUSALIB

Unlike in the previous study by Morten v. Lund the analysis in the present study is based on the ROOT based analysis framework AUSAlib[16]. AUSAlib is short for Aarhus Subatomic library and it is a toolbox formalising a lot of standard procedures in data analysis in experimental nuclear physics. The framework is developed in the nuclear physics group at Department of Physics and Astronomy at Aarhus University and the primary developers are Michael Munk, Oliver Kirsebom and Jesper Halkjær. As AUSAlib is continuously developed and usually a step ahead of the corresponding manual, Michael and especially Jesper have been of great help as patient gurus.

DECAYS

This thesis is concerned with β-delayed proton emission and coincidences between β-delayed protons and photons and hence this chapter is dedicated to an overview of the different relevant decay mechanisms.

This chapter is based on [13], [7] and [9].

2.1. β DECAY

Nuclei far from the valley of stability are generally unstable to reactions that bring them closer to stability. An example of such a reactions is the β^- decay which changes a neutron to a proton for nuclei near the neutron drip-line:

$$n \to p + e^- + \overline{\nu}_e \; . \tag{2.1}$$

Inversely for nuclei close to the proton drip-line the nuclei are unstable to β^+ decay or electron capture (EC):

$$p \to n + e^+ + \nu_e \tag{2.2}$$

$$p + e^- \to n + \nu_e \; . \tag{2.3}$$

Naturally, these reactions can only proceed if the Q-value; the energy released during the reaction, is positive. The Q-values for the reactions in equations (2.1)-(2.3) are

$$Q_{\beta^-} = M_Z c^2 - M_{Z+1} c^2 \tag{2.4}$$

$$Q_{\beta^+} = M_Z c^2 - M_{Z-1} c^2 - 2 m_e c^2 \tag{2.5}$$

$$Q_{EC} = M_Z c^2 - M_{Z-1} c^2 \; , \tag{2.6}$$

where M_Z and $M_{Z\pm1}$ are the masses of the mother and daughter nuclei respectively and m_e is the electron mass. Here the electronic binding energies have been neglected. As electron capture is mostly relevant near the valley of stability where β^+ decay is barely energetically allowed, electron capture will be omitted from the discussion here, even though ^{21}Mg lies in the proton rich region.

2.1.1. GAMOW-TELLER AND FERMI DECAYS

β decays are weak interactions and in the Standard Model of particle physics the weak interaction has a Lagrangian described mathematically by a V-A (vector minus axial-vector) structure. This interaction structure results in two types of allowed β-decays which for β^+ can be expressed as the two operators;

$$\hat{O}_F^+ = -\frac{G_F}{\sqrt{2}}\delta(\overrightarrow{r} - \overrightarrow{r}')T_- \tag{2.7}$$

$$\hat{O}_{GT}^+ = -\frac{G_F}{\sqrt{2}}\frac{g_A}{g_V}\frac{2\overrightarrow{s}}{\hbar c}\delta(\overrightarrow{r} - \overrightarrow{r}')T_- \ . \tag{2.8}$$

Here G_F is the Fermi constant, T_- is the isospin lowering operator, g_V and g_A are the vector and axia-vector coupling constants, and $\overrightarrow{s}$ is the spin operator. These two types of interactions are called Fermi (F) and Gamow-Teller (GT) and correspond to the vector and the axial-vector part respectively. The isospin lowering operator, T_-, changes the proton with isopin $T_3 = +\frac{1}{2}$ to a neutron with isospin $T_3 = -\frac{1}{2}$ in the β^+ decay. In the corresponding β^- decay operator the isospin lowering operator is replaced by an isospin raising operator, T_+. The delta function in the spacial coordinates specifies that the conversion of a proton to a neutron (or the inverse) happens at a certain space-point. The spin operator, $\overrightarrow{s}$, only occurs in equation (2.8) for the Gamow-Teller operator as only Gamow-Teller decays can involve nuclei with different spin. This is caused by the leptonic spin in the Gamow-Teller β decay being parallel and thus couple to one whereas in the Fermi β decay, the leptonic spins are anti-parallel and couple to zero. For the Gamow-Teller decays it then follows that the spin of the nucleus is allowed to change by one unit; $\Delta J = 0, \pm 1$ and $\Delta T = 0, \pm 1$. An exception is the $0 \rightarrow 0$ which is not an allowed Gamow-Teller β decay. Conversely, in the Fermi β decay where the total leptonic spin is zero, the spin of the nucleus is conserved; $\Delta J = 0$ and $\Delta T = 0$. Both types of β decays connect states with same parity. The above described constitutes the selection rules for β decay and due to this selection only a subset of the states in the β decay daughter are populated. This enables the analysis as the level density would otherwise be too high, especially at high excitation energies.

2.1.2. ft VALUES AND STRENGTH DISTRIBUTIONS

The ft value is the reduced transition probability of a β decay transition and as such a measure of the intensity of the transition. Here, t is the partial half-life of the transition; $t = T_{1/2}(I_\beta)^{-1}$, with $T_{1/2}$ the total half-life of the nucleus undergoing β decay and I_β the intensity of the specific β decay transition. f is the phase space factor and depends on the charge of the daughter nucleus and strongly on the maximum energy of the emitted β-particle. This means, that the phase space is much greater for decays to levels of low excitation energies in the daughter nucleus - where the energy of the emitted leptons is great - than for decays to levels of high excitation energy in the daughter nucleus. In terms of the nuclear matrix elements the ft value is given as

$$ft = \frac{C}{|M_F|^2 + \frac{g_A}{g_V}|M_{GT}|^2} \ , \tag{2.9}$$

with C a constant with a present value of $C = 6144.2(160)\,\text{s}$ and g_V and g_A the vector and axial-vector coupling vectors; $\frac{g_A}{g_V} = -1.2694(28)$[1]. $|M_F|$ and $|M_{GT}|$ are the Fermi and Gamow-Teller matrix elements respectively. In equation (2.9) small radiative and Coulomb corrections are neglected.

The selection rules for the Fermi decay described above causes the β decay strength associated with the Fermi interaction to contribute only to a population of the Isobaric Analogue State (IAS) in the daughter nucleus which has a similar structure and belongs to the same isospin multiplet as the initial state. The only difference between the mother and the IAS in the daughter nucleus is a neutron substituted by a proton or vice versa. This substitution causes a slight change in energy because of the Coulomb interaction; in a β^- decay the energy of the IAS increases by the Coulomb displacement energy as the new proton has Coulomb interactions with the original protons. Hence Fermi decay is only energetically allowed for β^+ decay. For Gamow-Teller decay there is no single favoured final state in the daughter nucleus because of the spin dependence of the interaction described by equation (2.8). Instead, the Gamow-Teller strength contributes to a lot of states resulting in a broad strength distribution with center in the so-called Gamow-Teller Giant Resonance (GTGR). The position of the Gamow-Teller Giant Resonance is also roughly determined by the Coulomb displacement energy and most of the Gamow-Teller strength is thus only accessible for the β^+ decaying proton rich nuclei. A schematic overview of the strength distribution is displayed in figure 2.1 for a neutron rich nucleus. The accessible states in the daughter nucleus are visualised as those within the Q_B window and for a neutron rich nucleus this does not include the IAS or the GTGR as it does for a proton rich nucleus. The states below the neutron threshold, S_n, in the daughter nucleus can only decay by emitting a photon and are hence very narrow. States above this threshold are broadened as they can also decay by particle emission.

The strong energy dependence of the phase space factor makes the relation between the partial half-life and the matrix elements in equation (2.9) strongly energy dependent too. That is, the strength distribution given by the matrix elements and the plot in figure 2.1 do not match the observed strengths as the phase space factor strongly favours the states at low excitation energy in the daughter nucleus.

2.2.   β-DELAYED PROTON EMISSION

The isobaric mass differences increase with increasing distance from the valley of stability towards the drip-lines and, furthermore, the binding energy of the least bound nucleon (or clusters) reduce. Hence as we approach the drip-line, more and more decay channels will be energetically allowed. Figure 2.1 for example illustrates the case of a neutron rich nucleus where the β-delayed one and two neutron emission channels are open.

The β-delayed particle emission spectra provide extended insight into the structure of the β decay daughter nucleus: Selection rules for the β decay puts constraints on the spin and parity of the fed levels in the β decay daughter. This is particularly handy for studying selected levels at high excitation energy in the daughter nucleus where the

---

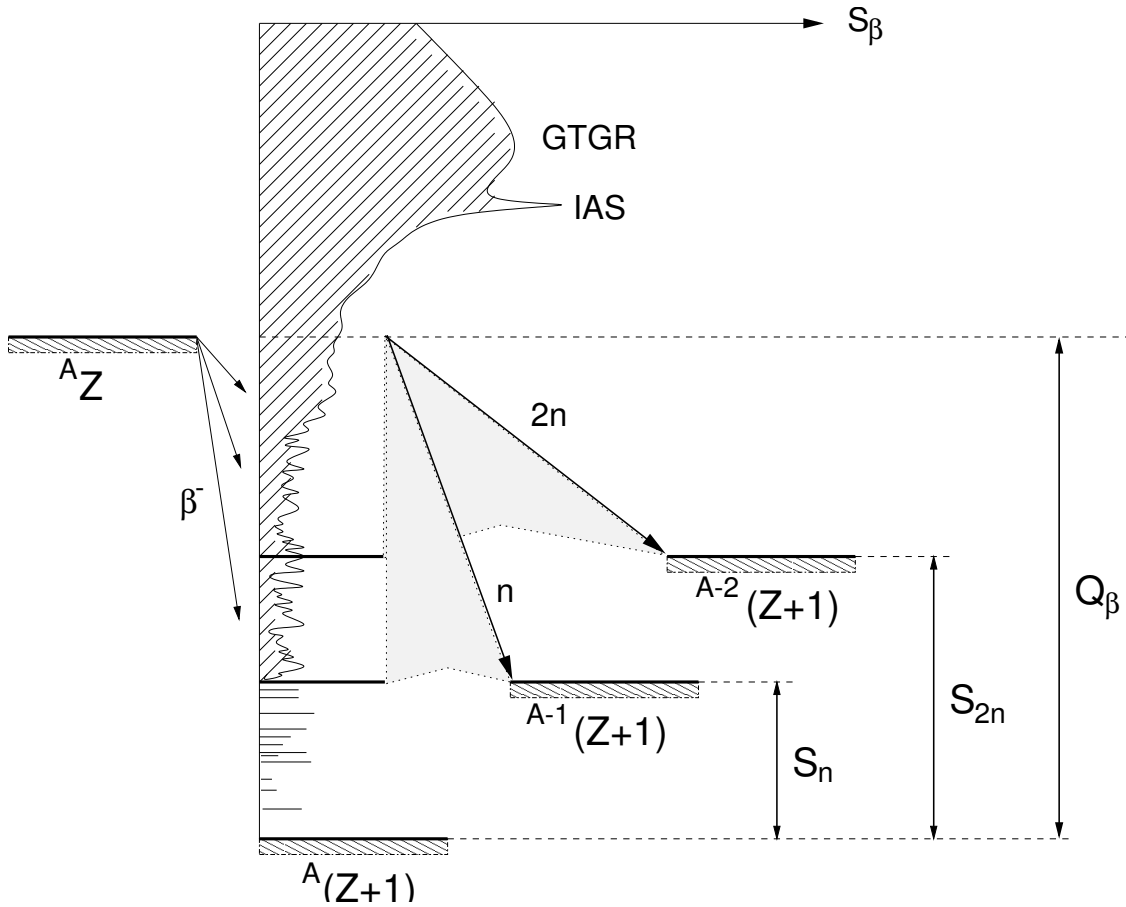[1]Values from February from Morten V. Lund [13].

Figure 2.1: A schematic view of the β decay strength distribution, S_β, for a neutron rich nucleus. The Fermi strength is accumulated in the IAS and the Gamow-Teller strength has a broad distribution with center in the GTGR. For proton rich nuclei IAS and GTGR will be located within the window of accessible states labelled by Q_β. The figure is inherited from Hans O. U. Fynbo [7].

level density is otherwise high. Including a subsequent particle and potential photon emission provides knowledge of the energy spectrum in the β decay daughter - and from this, decay branches can be placed accurately in the decay scheme. Studies of this sort are more readily available for proton rich nuclei than neutron rich nuclei as the emitted particles from proton rich nuclei have charge and hence can easily be detected with high resolution and efficiency. Moreover, for the proton rich nuclei the majority of the decay strength is accessible, which is not the case for the decay of neutron rich nuclei as outlined in the previous subsection. With decreasing distance to the drip-line more exotic decay branches open. These include multiple particle emission with subsequent emission of more protons or neutrons or even emission of clusters of nucleons as α particles. This project, however, is only concerned with β-delayed proton emission as other decay branches, though energetically allowed, have very low intensities and thus are negligible for this study of ^{21}Mg.

2.2.1. Coulomb barrier

When a nucleus decays by particle emission the nature of the decay depends strongly on the size of the Coulomb barrier compared to the available particle energy. In the present case where ^{21}Na decays by proton emission the Coulomb barrier can be calculated as

$$V(r) = \frac{zZe^2}{4\pi\varepsilon_0 r} \tag{2.10}$$

with e the elemental charge, z the atomic number of the escaping particle and Z and r the atomic number and radius of the proton emission daughter nucleus. The radius, R, of the nucleus can be estimated with the formula; $R = A^{1/3}r_0$, with r_0 approximately 1.4 fm. This gives a radius of $R = 3.8$ fm and in this case with a proton of $z = 1$ leaving behind a ^{20}Ne nucleus with $Z = 20$ the Coulomb barrier is estimated to be $V = 3.8$ MeV. This energy is located such that the decay of ^{21}Na by proton emission shows Q-values both below and above the Coulomb barrier. This will be shown in spectra in section 4.1. If the Q-value of the decay is larger than the Coulomb barrier the reaction proceeds as a Compound nucleus reaction with a relatively large decay probability. If on the other hand the Q-value is less than the Coulomb barrier the proton can only be emitted via tunnelling of the particle through the energy barrier. Tunnelling is less probable than compound nucleus reactions and as the resonance width is proportional to the decay probability this means that proton emission resonances with Q-values above the Coulomb barrier will be broader than those with Q-values below the barrier. This will be visible in spectra from this experiment in section 4.1. Another possible contributor to the barrier is the angular momentum. For nucleons bound in s-wave configurations the angular momentum is zero and there is no additional barrier due to angular momentum conservation. As the angular momentum increases in, for example, a d-wave configuration with $L = 2$ the energy barrier increases with an amount of approximately $1 - 2$ MeV. This reduces the transition probability for proton emission resonances with Q-values just a little bigger than the Coulomb barrier because these Q-values are now lower than the energy barrier when the angular momentum barrier is included. From the shell model, ^{21}Mg has a nucleon configuration with filled shells for the first 20 nucleons. The last nucleon has several possibilities but the configurations corresponding to lowest energy are for the nucleon to be in an s- or d-site. Thus s- and d-waves are the only ones we need to consider in this case.

Exceptions from the above described tendencies are the resonances corresponding to decays of the IAS in ^{21}Na. Even though these have high Q-values for proton emission the widths are relatively small due to oppression because the resonances are isospin-forbidden.

2.3. γ decay

When a nucleus is excited it can decay to a state with lower excitation energy or to the ground state by emitting a photon. These photons are electromagnetic radiation and thus governed by the electromagnetic force as opposed to the particle emission which relies on the strong interaction force. This means that photon emission will only contribute by a negligible amount to the total decay rate when particle emission channels are open and

therefore, γ decay is primarily relevant for energy states below the particle separation energy (see figure 2.1) or when the particle emission is heavily suppressed. The energy of the emitted photon is given by the difference in energy between the initial and final states except for a small amount of energy which goes to recoil of the decaying nucleus. However, this small contribution is often less than the uncertainty in the photon energy measurement and thus negligible which is also the case here.

As mentioned, the photons are electromagnetic radiation and an electromagnetic field which can be expanded in multipoles with each term classified by parity, π, and total angular momentum, L. The total angular moment consists of the orbital angular momentum and spin of the multipole - for a photon this is always 1. The electromagnetic field consists of both electric and magnetic field components and the multipoles can be split in electric and magnetic multipoles as well, with the electric being mainly connected to the charge distribution and the magnetic to the current density. Electric multipoles have parity $(-1)^L$ and magnetic multipoles have parity $(-1)^{L+1}$. The naming conventions are EL for electric multipole transitions with total angular momentum L, and ML correspondingly for the magnetic multipole transitions. The proton emission is dominated by the lowest order allowed multipolarity as the transition rate decreases heavily with increasing L. Furthermore, the transition strength is slightly larger for the electric multipoles than the magnetic resulting in the multipole E(L+1) contributing with an amount comparable to ML when these two are the lowest order multipoles.

2.3.1. SELECTION RULES

In a γ decay the angular momentum and parity are conserved quantities. Hence, a transition of multipole L, m between initial and final states with angular momenta J_i, m_i and J_f, m_f has to satisfy;

$$|J_i - J_f| \leq L \leq J_i + J_f \tag{2.11}$$

and

$$M_i - M_f = m \, . \tag{2.12}$$

The quantum number $L = 0$ corresponds to a monopole, $L = 1$ to a dipole, $L = 2$ to a quadrupole and so on. There are no monopole transitions as the monopole is a spherically symmetric and radially oscillating charge which at a distance corresponds to the potential of a fixed point charge. As the charge needs to be conserved this can not emit radiation. The parity conservation means that γ transitions for states with $\pi_i = \pi_f$ corresponds to even electric and odd magnetic multipoles - and vice versa.

EXPERIMENTAL METHODS

As mentioned previously, this project is based on data from an experiment performed in April 2015. The experiment to study the β-decay of ^{20}Mg was carried out at the ISOLDE facility [5] at CERN by the group of people who submitted the paper [15]. As the experiment was carried out almost a year before I started my project, I was not able to take part in the experiment myself. Hence for this chapter - and especially for section 3.2, I used the Ph.d. thesis of Morten V. Lund [13] as a valuable source of information. Morten was a member of the nuclear physics group at Aarhus University and hence has been reachable in case questions related to the experiment arose.

In this chapter includes a presentation of the ISOLDE facility in section 3.1, the detector setup is described in section 3.2 and in section 3.3 the mechanisms in energy loss of particles in matter is described as knowledge of such is necessary in order to be able to do a careful energy calibration. Calibrations of the various detector types are described in sections 3.5 and 3.6.

3.1. ISOLDE

The Ion Separator On-Line DEvice - better known as ISOLDE - is part of the CERN facility located across the border between Switzerland and France close to Geneva (with a fantastic view of the surrounding mountains in clear weather one might add). The CERN facility consists of more consecutive accelerators which together accelerate particles to velocities very close to the speed of light. The interconnected accelerator setup is illustrate in figure 3.1.

The total accelerator setup consists of LINAC's (LINear ACcelerator) feeding the Proton Synchrotron Booster (PSB) labelled BOOSTER in the figure and subsequently the Proton Synchrotron (PS). From there, the particles are guided to the Super Proton Synchrotron (SPS) and finally to the Large Hadron Collider (LHC). Along the way are several outlets where the beam is split such that some of the particles proceed towards the LHC and some are guided to other attached facilities. These facilities include ISOLDE which receives protons from the PSB. The PSB receives protons from the linac every 1.2 s and this bunch is split between the four synchrotrons stacked on top of each other which constitute the
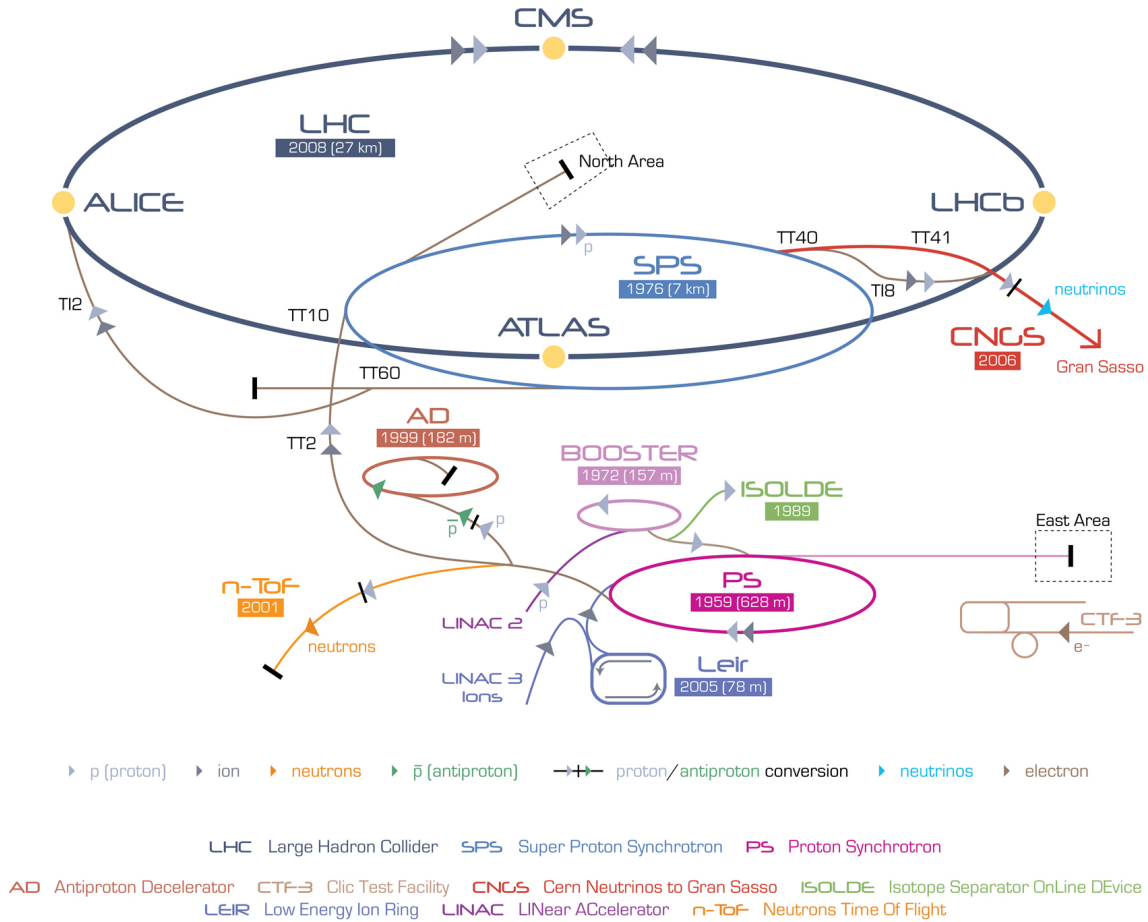
Figure 3.1: Schematic view of the CERN accelerator complex. A guide to the color codes is visible in the bottom of the figure - most importantly ISOLDE is marked with green next to the purple Booster and receiving protons marked with light grey. The figure is from [4] where it can be found in case of need to zoom.

PSB. In the PSB the protons are accelerated to $1.4\,\mathrm{GeV}$ and the four bunches are then collected and sent either to the PS or to the ISOLDE facility. In ISOLDE the protons are guided into the facility where they are implanted on the hot ion production targets. This is shown in figure 3.2 where we see the protons coming in from the left in the figure 3.2 and hitting two different targets. Both targets produce ions used for different experiments at the facility. The produced ions are then transferred by diffusion out of the production chamber and into the Resonant Ionisation Laser Ion Source (RILIS) where they are turned into singly-ionised ions. A fine tuning of the laser helps ionise only the desired ions and this improves the purity of the beam. Subsequently, the ions are extracted and separated by a mass separator to obtain a beam of the desired ions. This is where the setup with two ion production targets is relevant since the setup includes two mass separators; the General Purpose Separator (GPS) and the High Resolution Separator (HRS). Since the April 2015 experiment involved $^{20-21}\mathrm{Mg}$, the HRS was used as $^{20-21}\mathrm{Na}$ are very strong contaminants in both cases and have very similar masses. After the separator the ion beam is guided
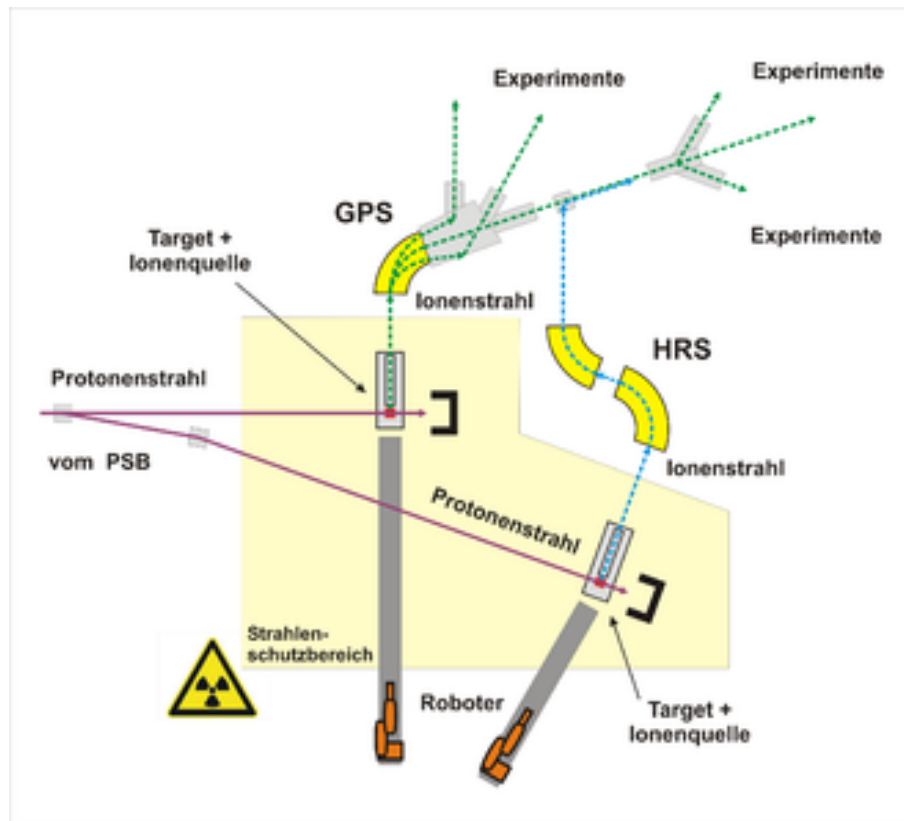
Figure 3.2: The figure shows the beam production target and beam separators. Doing experiments at ISOLDE involves being part of an international research community - and in this light, I hope the reader will bear with me for using a single figure in German.

to the detector region which in the case of the April 2015 experiment was located at the ISOLDE Decay Station (IDS).

3.2. DETECTOR SETUP

The ISOLDE Decay Station (IDS) was used as setting for this experiment to take advantage of the array of four HPGe Clover detectors, which is part of the setup at the IDS. Each of the clover detectors consists of four High Purity Germanium crystals - hence the name. The HPGe-detectors were arranged around the heart of the setup as shown in figure 3.3a. The vacuum chamber surrounded by the HPGe-detectors contains an array of Si-detectors and a carbon foil, where the ^{21}Mg ions are implanted. These parts are fixed in a 3D-printed structure as shown in figure 3.3b. The dimensions of 3D-printed structure are known to high precision; a hundredth of a millimetre, which is an advantage in making a reliable geometry calibration.

(a) The HGPe-detectors surround the rest of the setup to measure the outcoming photons, which easily penetrate through the inner parts of the setup.
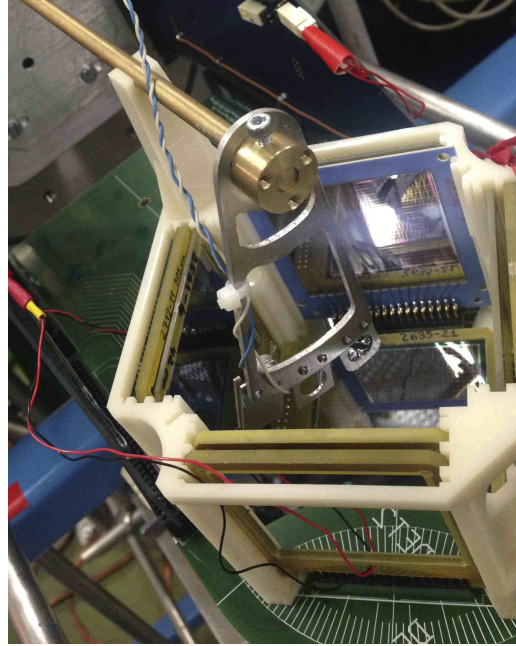
(b) The Si-detectors are placed in telescope configuration in a 3D-printed structure.

Figure 3.3: Fotos of the experimental setup at ISOLDE Decay Station. The fotos are taken by Morten V. Lund and also appears in his dissertation [13].

3.2.1. DETECTOR TYPES

In the setup of the April 2015 experiment several different detector types were used. HPGe detectors detected the escaping photons and silicon detectors captured the emitted charged particles. More types of Si-detectors were used; unsegmented pad detectors and segmented strip detectors. Figure 3.4 shows a depiction of a detector with the straightforward name Double Sided Silicon Strip Detector (DSSSD). As the name describes this type of silicon detector has strips on both front and back side. The 16 strips on the back are perpendicular to the 16 strips on the front forming an array of 256 segments with separate readouts. Aside from the DSSSDs the segmented detectors in this setup include a Silicon Strip Detector (SSD) with strips on a single side. Both types of strip detectors have strips of width 3.0 mm and an interstrip width of 0.1 mm. When a particle hits the detector between the strips no signal is detected. Hence, from the unsegmented pad detectors all the hits are pooled together whereas the strip detectors (DSSSDs and SSD) store information on where in the detector, the signal originated. When the detection spot is specified a more precise characterisation of the charged particle path is possible, and then a more precise calculation of energy loss through the detector material can be made. I shall elaborate on the energy loss in section 3.3.

Figure 3.4: Drawing of a DSSSD with 16 strips on the front and 16 perpendicular strips on the back, which in total forms a detector with 256 separate segments. Figure from [13].

3.2.2. SETUP

The silicon detector setup consists of five Double Sided Silicon Strip Detectors (DSSSDs) of different thickness, a single sided Silicon Strip Detector (SSD), and three pad detectors which have no strips. Except for the thickest of the DSSSDs the Si-detectors are arranged in different charged particle telescope formations with one detector positioned in front of another both facing the foil in the center. This setup enables different constraints on the spectra as described in section 4.3. A setup which includes detectors of different thickness in different configurations is an advantage as the thicker detectors has better energy resolution and usually less noise than the thinner detectors. In turn, the thinner detectors collect less positrons from β decays and thus have visible peaks at lower energies.

Figure 3.5 s generated using the SetupEditor which is a build-in tool in the AUSAlib framework. The figure shows the experimental setup graphically with the beam coming from the bottom of the picture and hitting the carbon foil labelled F. Letters A-D label different charged particle telescopes. At position A is a telescope with a $20\,\mu$m SSD (U2) in front of a $500\,\mu$m DSSSD (U1). A silicon detector of $20\,\mu$m can bring protons with an energy of op to $1152\,$keV to a complete standstill by means of electronic and nuclear stopping of the charged particle in the material. This is calculated with a handy energy loss calculator tool [8] made by Jesper Halkjær based on SRIM-13 tabulations [20]. Except for some edge effects - primarily due to the fact that the particles do not always take the straight perpendicular path through the detector and hence often traverses more than $20\,\mu$m of silicon - protons with energy higher than the $1152\,$keV limit will punch through the U2 detector and be absorbed in U1. This proton punch through energy depends of course on the thickness of the material and will be different in the different telescope configurations. The letter D indicates the position a telescope with a $40\,\mu$m DSSSD (U4) in front of a $500\,\mu$m pad detector (P1). The proton punch through energy for U4 is $1803\,$keV, so particles with energies up to a maximum of $1803\,$keV will be visible in the U4 energy spectrum. Likewise, B is a telescope consisting of a $60\,\mu$m DSSSD (U3) in front of another $500\,\mu$m pad detector (P3). The $60\,\mu$m Si-detector stops protons with a maximum energy of $2321\,$keV. The telescope at C has a $300\,\mu$m DSSSD (U6) in front of yet another $500\,\mu$m pad detector
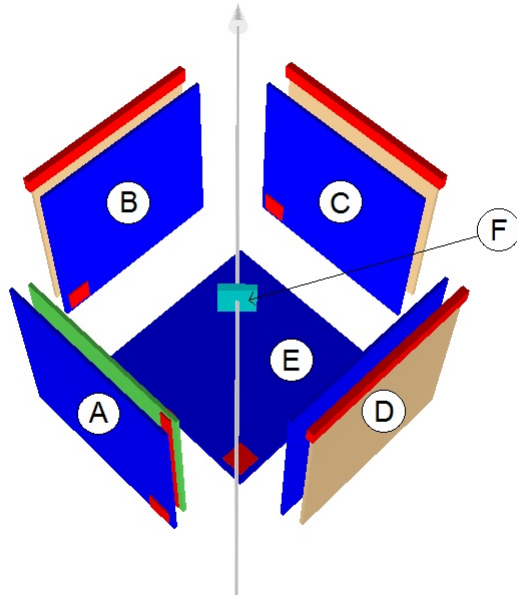
Figure 3.5: This graphical depiction of the experimental setup is generated with the SetupEditor which is build in as a tool in AUSAlib and on the basis of the same setup-files as was used for calibrating the setup. The letters A-E label silicon detectors with A-D being telescope configurations. F label the carbon foil. (The letter-labelling was done manually.)

Name	Type	Thickness [μm]	E_p [keV]	Ω_{det} [%]
U1	DSSSD	500		4.69 (10)
U2	SSD	20	1152	5.21 (12)
U3	DSSSD	60	2321	5.19 (12)
U4	DSSSD	40	1803	5.33 (12)
U5	DSSSD	1000		6.31 (15)
U6	DSSSD	300	6109	5.63 (14)
P1	pad	500		4.69 (10)
P2	pad	500		4.71 (11)
P3	pad	500		4.57 (10)

Table 3.1: Information on the thickness and dead layers of the different detectors. The proton punch through energy E_p is provided for the detectors positioned as the front in a telescope.

(P2). Compared to the three other telescopes, this front detector is very thick and proton will have to have en energy exceeding 6109 keV to punch through U6. The last Si-detector is the 1000 μm DSSSD, U5, located at the letter E in figure 3.5 and facing upward. The details about thickness are summarized in table 3.1 along with the energies, E_p, required for a proton to punch through the front detector of the listed thickness according to [8]. Table 3.1 also includes the solid angle coverages for the respective detectors.

The red markers in figure 3.5 show how the strips are counted. Of course, the beige pad detectors in the back of the telescopes at B-D have no strips, so the red marker on

those just checks the orientation. The green SSD (U2) in the front of the telescope at A has a vertical red strip. This shows the location of strip number one and it is thus visible that the vertical front strips are numbered from the left when viewed from the center of the setup. The blue DSSSDs have strips on front and back: The front strips are vertical and counted from the left just as for the SSD. The back strips are horizontal and numbered from the bottom. Therefore, the marker is placed in the bottom left corner of the DSSSDs when viewed from the center to mark the placing of segment 1.1. It is important to be aware of the orientation when doing the geometry calibration.

3.3. ENERGY LOSS OF PARTICLES IN MATTER

Knowledge of how the different kinds of emitted particles lose energy when propagating in the setup is crucial for this kind of experimental work. The detectors measure energies and intensities of the particle radiation and interpretation of these measurements are the results. Hence, it is important to know how the setup and other factors influence the readouts from the detectors.

There are three different kinds of particles we need to consider in this study; the uncharged photons, the charged electrons from β-decay and the heavier charged protons.

3.3.1. PHOTONS

Photons generally interact little with any matter it traverses and thus it is no problem to have the HPGe-detectors surrounding the rest of the experimental setup. For completeness, nevertheless, an overview of the most dominant energy loss processes for photons will follow in this paragraph. These processes include the photoelectric effect, pair production and Compton scattering, each of which are dominant in a specific energy region. The relevant photon peaks in this study are located at energies ranging from approximately $1.5\,\mathrm{MeV}$ to $6\,\mathrm{MeV}$ and with this information figure 3.6 can be used to determine which process is more dominant. Figure 3.6 is from [6]. Since the setup consists of more light materials (silicon has $Z = 14$) part (a) of figure 3.6 is the more reliable representation of the energy loss because the light material carbon ($Z = 6$) more accurately resembles the actual material than the heavier lead ($Z = 82$). Figure 3.6 shows cross section for interaction as a function of photon energy - both the total cross section and contributions from different processes are shown with abbreviations:

- $\sigma_{p.e.}$: photoelectric effect
- $\sigma_{Rayleigh}$: Rayleigh scattering
- $\sigma_{Compton}$: Compton scattering
- κ_{nuc} : pair production caused by nuclear field
- κ_e : pair production caused by electronic field
- $\sigma_{g.d.r.}$: giant dipole resonance

Here, as mentioned, I shall touch upon the photoelectric effect, Compton scattering and pair production as these three processes primarily govern the course of the combined total cross section for carbon.
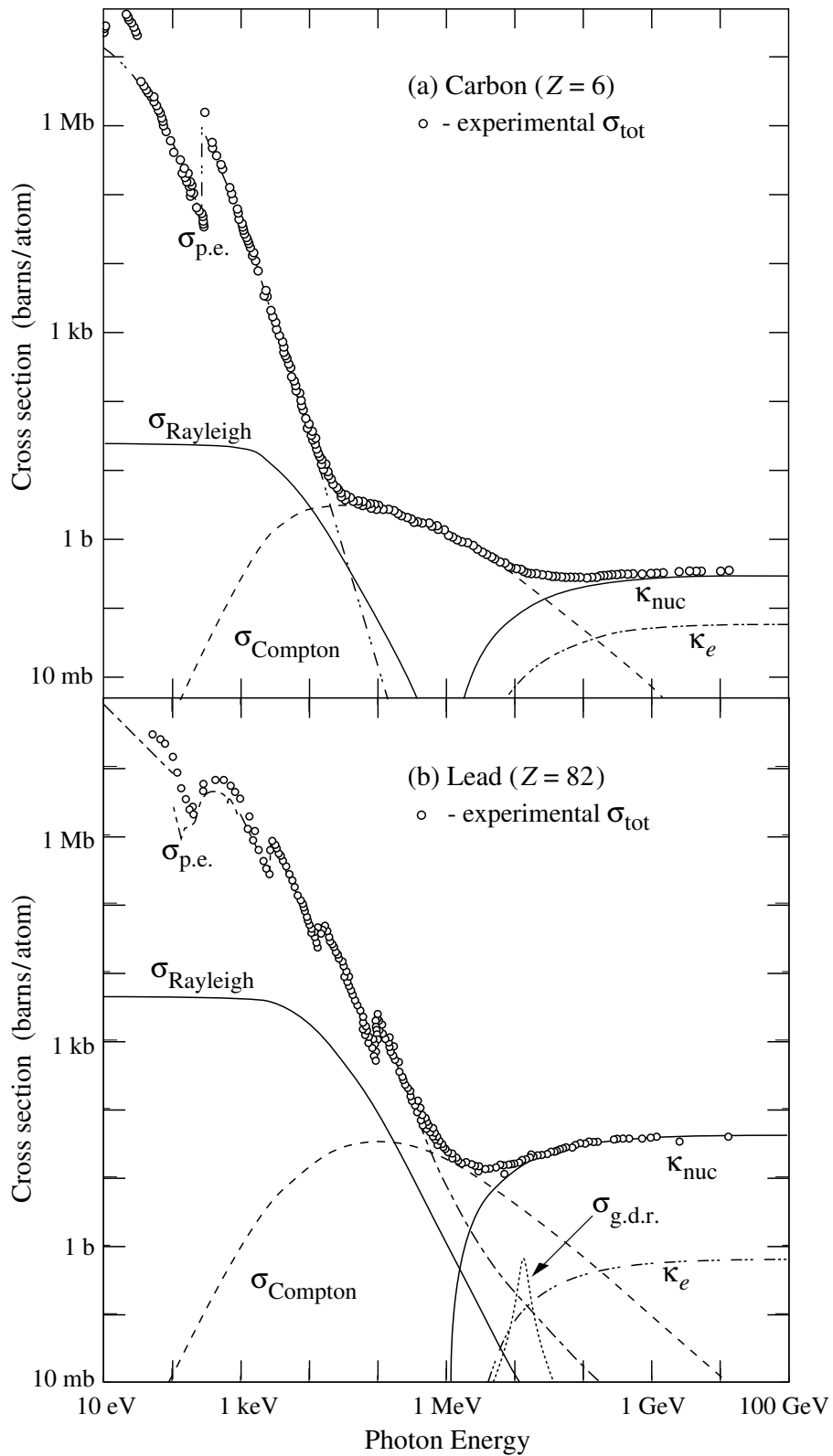
Figure 3.6: Classic figure which shows the contribution from different effects to the stopping of photons. From [6]

Photoelectric effect is a low energy phenomena where a photon transfers its entire energy to an atomic electron which causes the electron to exit its orbit around the nucleus and continue as a free electron. The discontinuities in the graphs in figure 3.6 where $\sigma_{p.e.}$ dominates are called absorption edges. These are located at energies specific for the absorbing material and indicate when a threshold for photoionisation of a new level is reached.

Pair production is the conversion of energy to a particle-antiparticle pair; typically - as here - referring to the conversion of a photon to an electron-positron pair. In order for pair production to be possible the energy of the photon needs to exceed the threshold of the combined rest mass of the electron and positron which is 1022 keV and pair production is thus only relevant for high photon energies. Like any other reaction, the pair production has to conserve quantum numbers, energy and momentum. Conservation of quantum numbers is assured by the particle pair consisting of an elementary particle and its own antiparticle - as is always the case. Energy and momentum could not be conserved at the same time if the pair production was to take place in free space, so the process only occurs i the vicinity of another particle which can receive some recoil energy. As visible from figure 3.6 the cross section for pair production is larger off of a nuclear field than an electronic field. Similarly, the probability of the process also increases with the atomic number of the nucleus making the cross section for pair production visibly larger for lead than for carbon.

The most significant energy loss process for photons in the energy range relevant for this study is the *Compton scattering*. Compton scattering is inelastic scattering of photons by a charged particle - usually an electron in an atom. This process is at photon energies much larger than the binding energy of the electron and thus the electron can be considered free. Each inelastic scattering reduces the energy of the photon a little and the photon will often undergo multiple successive scatterings. This creates a continuous distribution of photon energies which, if the photon had not undergone any scattering, would have all belonged to a full resonance peak. Instead the photons with reduced energies now form what is called a Compton edge. In figure 3.7 a spectrum of all photon energies obtained in the experiment is shown. In this graph some of the mentioned Compton edges are visible at approximately 1200 keV and 2350 keV. These edges are results of Compton scattering of photons with energies originally belonging to the peaks just above the edges in energy. The amount of photons scattered depends on the cross section for the process - and incorporating knowledge about scattering cross sections into the calibration of the detectors one can counter the non-linear scattering effect.

3.3.2. CHARGED PARTICLES

Charged particles also lose energy when they travel through matter due to interactions with electrons and nuclei in the material. Then the projectiles undergo electronic energy loss it results in excitation or ionisation of atoms in the material, whereas nuclear energy loss is the transfer of energy to center of mass movement of atoms in the material. The amount of energy lost by the particle can simply be described by the following equation [19];

$$\langle \Delta E \rangle = N \cdot \Delta x \cdot \sigma \,, \tag{3.1}$$
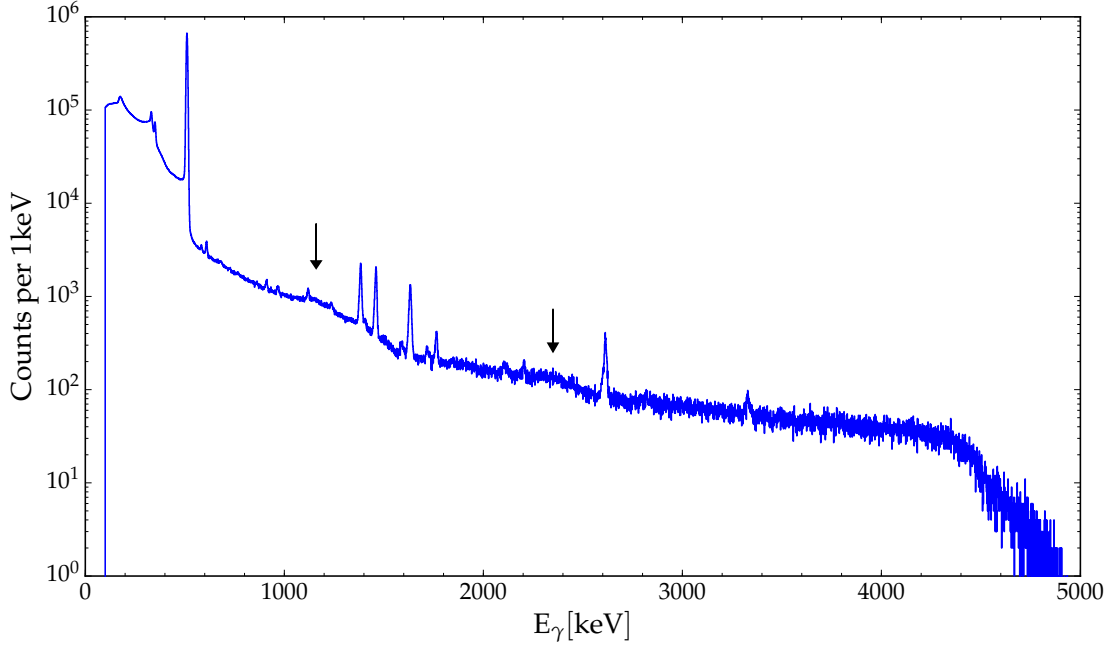
19

Figure 3.7: All photon energies displayed. The graph includes all energy readouts from the detectors C1, C2, C3 and C4 which are the HPGe clover (hence C) detectors.

where $\langle \Delta E \rangle$ is the average amount of energy lost over the distance Δx, when there are N particles per volume to scatter the projectile and the cross section for interaction with one of these is σ. σ is inversely dependent on the mass of the scattering particles, and as the mass of a nucleus is much larger than that of an electron, usually $\langle \Delta E \rangle_n \ll \langle \Delta E \rangle_e$. This is true unless the projectile is very slow so the binding energy of the electrons is comparable in size. This implies that the stopping of energetic projectiles causes several atomic electrons to be emitted resulting in contamination of detected data.

A more advanced formula for energy loss of charged particles of high velocity in matter was presented by Hans A. Bethe in 1930 [19]:

$$\frac{dE}{dx} = 4\pi N Z \frac{z^2 e^4}{m v^2} \left[\ln \left(\frac{2\gamma^2 m v^2}{\hbar \langle \omega \rangle} \right) - \frac{v^2}{c^2} \right] . \tag{3.2}$$

Here $\frac{dE}{dx}$ is the amount of energy lost over an infinitesimal distance, N is the number of atoms per volume, Z and z are the numbers of electrons in the target material and projectile material respectively, m is the mass of the target and v is the velocity of the projectile. ω is the angular frequency of the orbital motion of the target electron around its nucleus, γ is the Lorentz factor, $\hbar$ is the reduced Planck constant and c is the speed of light in vacuum. Bethe's stopping formula improves Bohr's classical stopping formula by including quantum mechanics to make it valid for particles with high velocities. Taking quantum mechanical effects into account is especially relevant for close collisions between projectile and target. Bethe's stopping formula in its form in equation (3.2) applies to light charged particle projectiles as protons or α-particles but not electrons. The formula
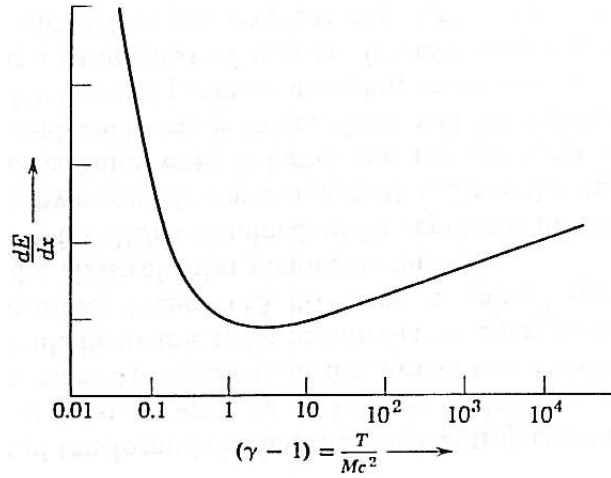
Figure 3.8: Graphic representation of the Bethe stopping formula (3.2). From [19].

is depicted in figure 3.8 with T the kinetic energy and M the mass of the projectile. For low energies the logarithm $\ln\left(\frac{2\gamma^2 m v^2}{\hbar\langle\omega\rangle}\right)$ varies only slowly and thus $\frac{dE}{dx} \propto v^{-2}$. At higher energies the course of the graph changes and as the velocity approaches the relativistic limit the logarithmic part becomes dominant and $\frac{dE}{dx} \propto \ln\gamma$ for $\gamma \gg 1$. These tendencies in different kinetic energy regimes are visualised in figure 3.8. There are numerous corrections to the Bethe formula in equation (3.2) both for low energies in the classical limit and for high energies. In the relevant energy regime for this study the uncorrected Bethe formula gives an acceptable impression of the stopping and thus I shall not go into detail about the corrections. Nevertheless, the SRIM stopping tables [20] used in stopping calculations in this study of course incorporate the Bethe formula with all of the related corrections in both the low and high energy end.

When considering the propagation of charged particles in matter another important concept is range. The range is the distance the particle can traverse before brought to a complete standstill and thus is closely related to the stopping relations for the different particles. As per equation (3.1) the range, R, is thus given by

$$R = \int_0^{E_0} \frac{1}{N \cdot \sigma(E')} dE' \,, \tag{3.3}$$

where E_0 is the initial energy of the penetrating particle and $\sigma(E')$ reminds us, that the scattering cross section is dependent on the energy of the particle. The range of a particle is not an absolute determined size. Since the penetration of the particle into matter involves multiple scatterings there will be some deviation in the penetration depth. This is called straggling and causes the total penetration depth of the particles to be approximately Gaussian shaped around the calculated range. With equations (3.1) and (3.3) both energy loss and range can be calculated based on knowledge on traversed distance and initial energy respectively. Both of these aspects will be utilized in the following paragraph on thickness of dead layers and the carbon foil.

The final note on energy loss before using all of these concepts for data analysis concerns

the change in direction of the charged particles as a result of multiple scattering events. Lighter electrons undergo greater dispersion as a result of the Compton events than the heavier protons. In the segmented detectors this means, that the electrons are likely to deposit energy in more than one strip. This causes a considerable contamination by electrons in the detector readouts, but as this study is not concerned with electron energies this is of less importance. If a proton scatters within the detector material it will generally stay within the same strip unless it hits very close to the edge of the strip - in this case it might contribute some energy to the inter strip region where the energy is not detected. If the protons scatters but stays within the same strip it will be read out as one detected event.

For energy loss calculations in this study I use the energy loss routine [8] that is based on SRIM (Stopping Range In Matter) tables [20]. These tables are constructed on the basis of Monte Carlo simulations with multiple scattering events and assuming the particles propagate on straight lines between the successive scattering events in the material. Given the type and energy of the incoming projectile and the composition of the target material SRIM will then provide a table of stopping powers, range and straggling as a function of the energy of the incoming projectile.

3.3.3. THICKNESS OF DEAD LAYERS AND CARBON FOIL

The charged particles in this experiment propagate out of the carbon foil in which the decay processes that produce them take place and afterwards they traverse a few centimetres of free space and strike the detectors. Thus, they only lose energy in the carbon foil and the dead layer on the front of the silicon detectors before depositing their energy which is read out as data. As motivated above, it is thus crucial to know the thickness of these obstacles in order to be able to translate between the energy measured in the detector and the center of mass energy which the charged particle originally had when emitted in the reaction. Accounting thoroughly for these energy losses is important as the resulting energies are never more accurate than the weakest and most inaccurate points in the analysis.

Morten V. Lund determined the thickness of the carbon foil [13] and I inherited his result of this analysis which I shall outline here. The carbon foil thickness was determined with an α-source (^{148}Gd, ^{239}Pu, ^{244}Cm) in a vacuum chamber at Aarhus University. The α-source produced a spectrum of peaks with well-known energies and the peak positions after passage of the carbon foil was different by an amount signifying the amount of carbon the particles traversed prior to detection. The energies of the four calibration peaks are $3182.690(24)$ keV, $5156.59(14)$ keV, $5762.64(3)$ keV and $5804.77(5)$ keV. Morten then calculated how much the peaks would shift in energy for 200 different carbon foil thicknesses. Comparing the difference between the result of these simulated spectra and the data for the α-particles through the actual carbon foil with a χ^2-test revealed the thickness of the carbon foil to be

$$d_{carbon} = 109(2)\,\text{nm}\,. \tag{3.4}$$

Of course the emitted particles do not have to traverse all of this as the decay of the ^{21}Mg happens inside the foil and not before. The impact depth of the 30 keV ^{21}Mg-beam into the carbon foil was calculates with SRIM to be 44.8 nm and the emitted particle only lose energy from passage of the remaining part of the carbon foil.
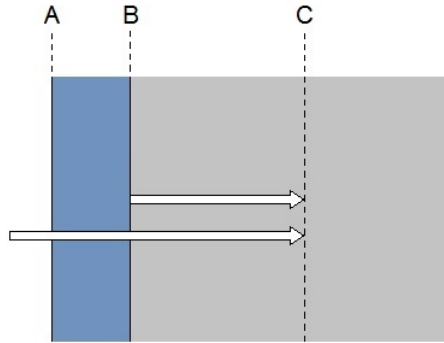
Figure 3.9: Illustration of a silicon detector with dead layer. The blue part signifies the dead layer.

The thickness of the dead layer on the respective silicon detectors are given by the manufacturer. The dead layer is the outermost layer on the front and back of the detector where a penetrating particle deposits energy which does not reach the detector channels. Hence the energy is being attenuated as a consequence of the passage of the dead layer. Figure 3.9 is meant to illustrate the reversed engineering process to reconstruct the energy of the particle before penetration of the dead layer. When the particle arrive at the edge of the detector dead layer, A, it has energy E_A and the range $R_A = |AC|$. After passage of the dead layer at position B, the particle has energy $E_B < E_A$ and a projected range $R_B = |BC|$. The energy lost in the dead layer is not read out by the detector, and thus the energy deposited in the detector by a particle with initial energy E_A is E_B. Utilizing the given values for dead layer thickness and the relations between penetration depth and energy given by SRIM one can then calculate E_A from E_B: First determine the projected range R_B a particle of a specific type with energy E_B would have in the specified material. Then adding the dead layer thickness to this range; $R_A = R_B + |AB|$. Finally reversing the tables and determining the energy the particle needed to have in order to penetrate a distance R_A into the material. Such calculations based on SRIM tables are incorporated in the AUSAlib routines which are used for the data analysis.

Dead layer thickness for each detector is displayed in table 3.2 along with type and thickness of each detector.

3.4. DATA

I received the raw data as ROOT files. ROOT is a data analysis framework facilitated by CERN [1]. The ROOT files are consecutively numbered and each file contains data from many events in the detectors but still from the same measurement. When the limit for how much each file can store (200 MB) is reached a new file is created. The data in the files is structured as a so-called TTree of type h101 each with 39 branches. The branches contain data saved for each individual electronic channel in the data acquisition system. For this experiment seven ADC modules and four TDC modules were used where the ADC

Detector	Type	Thickness [μm]	Dead layer [μm][a]
U1	DSSSD	500	0.1 ; 0.6
U2	SSD	20	0.5 ; 0.6
U3	DSSSD	60	0.1 ; 0.6
U4	DSSSD	40	0.1 ; 0.6
U5	DSSSD	1000	0.1 ; 0.6
U6	DSSSD	300	0.1 ; 0.6
P1	pad	500	0.6
P2	pad	500	0.6
P3	pad	500	0.6

Table 3.2: Information on the thickness and dead layers of the different detectors.

[a]where two numbers are specified (xx ; yy) xx indicates the dead layer on the frontside, and yy is the dead layer on the backside. Only one number means dead layer on the frontside as the backside dead layer is not of relevance.

modules handle the energy signals and the TDC modules handle the time signals. In each TTree there are thus branches named Mx, MxI, MxE signifying signal from ADC module x for x = 1, 2, 3, 4, 5, 6, 7. Here Mx is the multiplicity of an event, MxI is a vector of length Mx containing the channel number and MxE is a vector of equal length containing the corresponding energies. The time data from the TDC modules have the same structure; Tx, TxI, TxE with x = 1, 2, 3, 4 containing time signals belonging to the same events as the corresponding energy data. In addition to the 33 ADC and TDC branches there are six branches with collective data related to all the ADC and TDC event stored in the file. Most of these are irrelevant for the present analysis of this kind of decay experiment, so only the branch labelled TPROTONS is worth mentioning here. TPROTONS store all data for hits in the silicon detectors versus time. The reason for the name TPROTONS is, that the ^{21}Mg beam is produced by a proton beam on a production target and this proton beam is possibly renewed every 1200 ms. If the beam is renewed, the time will be reset to zero. The TPROTONS spectrum will be used for determining the half-life of ^{21}Mg in section 4.2.

A *mapping* of data translates the ADC/TDC structure to a structure where data is arranged according to which detector and which strip was hit in the event. The 70 different branches in the h101 TTree of mapped data are now labelled

  – Silicon strip detector (both DSSSDs and SSD) with x = 1, 2, 3, 4, 5, 6:
     UxF, UxFI, UxF_E, UxF_T
     UxB, UxBI, UxB_E
  – Silicon pad detectors with x = 1, 2, 3:
     PxE, PxT
  – HPGe Clover detectors with x = 1, 2, 3, 4:
     Cx, CxI, CxE, CxT

UxF, UxB, and Cx contain multiplicities which is the number of segments hit during one readout. A large multiplicity often signifies a lot of noise. UxFI, UxBI and CxI contain

vectors of lengths specified by the corresponding multiplicities and tell which segment was hit by how many particles. These two categories of branches are of course only relevant for the segmented detectors. UxF_E, UxB_E, PxE and CxE present the energies of the hits and similarly, UxF_T, PxT and CxT provide the corresponding times for the hits. There is no need for the time readout from the back strips in the silicon strip detectors as this would be identical to UxF_T. For the segmented U and C detectors the energy and time branches will also contain a vector with the same number of entries as the multiplicity. To clarify; a readout will be triggered when a detector is hit with a sufficient energy but the readout does not happen instantaneously and thus, more hits has time to strike the detectors and those will then be stored as part of the same event. The finite length of the readout is the reason for the high multiplicities in one event.

In order for the data to have a structure suited for AUSAlib, it was processed through the *Sorter* from the AUSAlib library. The Sorter matches, calibrates and rewrites the data in AUSAlib format. The matcher file gives some global options for the DSSSDs and SSD including a possibility of excluding defect strips. In order to work with data and test and renew the calibrations I ran the Sorter without the calibration files first. After generating and adding the calibration files the Sorter was implemented again on the mapped data to incorporate the calibration.

3.5. CALIBRATION OF THE SI-DETECTORS

The ^{21}Mg isotope which the present study is based on was originally just meant to serve as an in-beam calibration source for the ^{20}Mg experiment. In-beam calibration is often preferred if possible as more reliable geometry calibrations can be made from experiments where the target is not moved or changed in the middle of the experiment. If the calibrations are based on data from a stationary α source, which is also common practise, the α source has to be placed in the target ladder instead of the carbon foil and wherever human hands interfere there is a risk of additional error. A reason for choosing ^{21}Mg as calibration source over ^{20}Mg is that ^{21}Mg is a little closer to stability than its mass-20 sister isotope which means that ^{21}Mg is easier to produce and preserve in large amounts and thus easier to work with. Moreover, ^{21}Mg has strong β-delayed decay modes from ^{21}Na to ^{20}Ne with well documented energies. In resent studies it has been reinterpreted [13] which levels these decays connect in ^{21}Na and ^{20}Ne but the precision on the energies are not questioned. For these reasons ^{21}Mg was used for calibration where it was possible - which is for all silicon detectors but the thinnest strip detectors; U2 ($20\,\mu$m) and U4 ($40\,\mu$m). U2 and U4 are so thin that most β-delayed protons punch directly through them. Instead the calculations of these two detectors are based on the β-delayed α-particles from the decay of ^{20}Na which was available with the ^{20}Mg beam.

If I have learned something from the last months it is that making good calibrations is a time-consuming process if you are determined to be thorough. The best way of utilizing the time in this project has thus been to check the available calibrations from Morten V. Lund's study [13], familiarize myself with the procedures and seek to improve he energy calibrations only for a few selected DSSSDs.

The calibrations I inherited from Morten V. Lund were created for an analysis without the AUSAlib frame work. Hence, even for the calibrations which I have not changed, an understanding of the involved methods and outcome has been important to obtain in order to recast the calibrations correctly in AUSAlib format. For this purpose, I have familiarized myself with the .json and .cal types of files and modified some existing template files to suit this experiment. The .json and .cal files include setup.json, target.json and a .json and .cal file for each detector. These files contain all the knowledge required to process the data: The setup.json file takes all the detector.json and detector.cal files as input and specifies position and orientation of the detectors. Furthermore, setup.json determines the labelling of the different output branches for each detector - U3F_E for instance. The detector.json files hold information about strips, thickness and dead layer and detector.cal contains the calibration coefficients. Equivalently, the target.json file has the position, orientation and measurements of the target.

3.5.1. Geometry calibration

The geometry calibration used here is the one I received from Morten V. Lund from his work with the ^{20}Mg data from the April 2015 experiment. I have familiarized myself with the applied methods but not reproduced the calibration, and this subsection serves to communicate my acquired knowledge.

As described in section 3.3, particles lose energy when penetrating through matter. This is why a precise knowledge of the geometry of the setup is crucial in order to be able to calculate accurate energies as the particles propagate towards the detectors. For some parts of the geometry calibration we rely on the accuracy of the 3D-printed structure which keeps the Si-detectors in place as shown in figure 3.3b. The 3D structure is sufficiently accurate for determining the distance, z_0, from the foil to the Si-detectors as the particles propagate through vacuum over this distance. Hence there are practically no collisions with other particles over this distance and the distance is merely interesting because the intensity of the radiation gradually decreases with distance from the source. On the other hand, the distance traversed through the dead layer of the detectors is very important as motivated in section 3.3. Thus the exact center points of the radiation on the detectors have to be determined to higher precision. I shall here distinguish between what I shall call the *geometric center* of the detector front - which is the midpoint if measured by a ruler and will be labelled $(x, y) = (0, 0)$ - and the *intensity center* which will designate the center of the detector with regards to the particle radiation from the reactions in the carbon foil. The location of the intensity center is labelled by (x_0, y_0) and can be offset by a few millimetres relative to the geometric center. Reasons for this offset include small misalignments in the target and/or the beam which are difficult to completely eliminate. The position of the intensity center is determined by analysing hit patterns from the in-line calibration source. The decay of ^{21}Mg and ^{20}Mg has no preferred direction in space and thus is isotropically distributed. Due to the intensity decreasing with distance from the source the hit pattern will then reveal the point on the detector which is closer to the source; the intensity center. When this is known the distance from a pixel to the intensity center
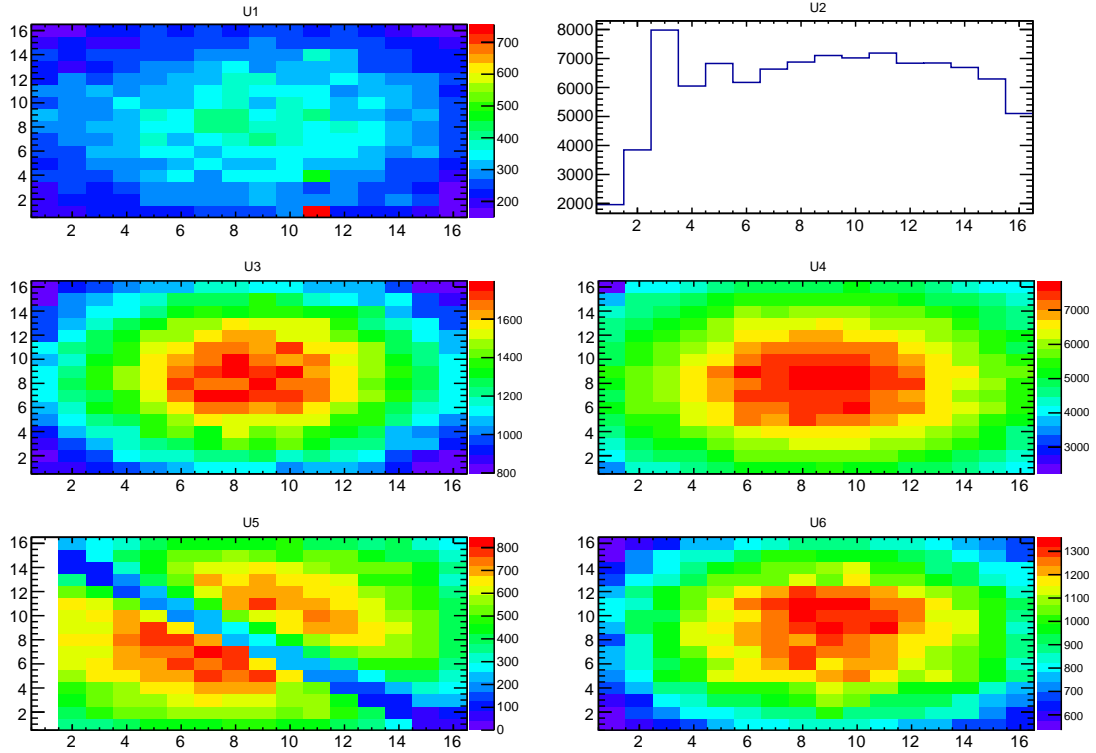
Figure 3.10: Beam spots on the silicon detectors with calibration sources; protons from the decay of ^{21}Mg for detectors U1, U3, U5 and U6 and α-particles from the decay of ^{20}Mg for the thin U2 and U4. Front strips are on the horizontal axes and back strips are along the vertical axes for the DSSSDs.

can be determined and then the angle of incidence between a particle and the detector can be calculated. This then in turn gives the actual dead layer thickness the particle has to traverse to strike the detector and is for this reason important for the energy calibration.

The hit patterns in the six strip detectors are shown in figure 3.10. Detectors U1, U3, U4, U6 have well centered two dimensional beam spots. U2 is a single sided detector and thus have only a one dimensional intensity distribution. The hit pattern in U5 looks irregular due to the horizontal position of the U5 detector underneath the target ladder (see figure 3.5). The target ladder shields along the diagonal of U5 and thus the blurring in the beam spot was expected. The position of the intensity center was determined by fits to the hit patterns and the result is summarised in table 3.3. The 3D-printed setup structure arrange the detectors in telescope configurations aligned with respect to the carbon foil in the center. Due to this positioning the beam spot position of the respective front detectors are adopted for the pad detectors as well. U2 is the front detector in a telescope with U1 and unfortunately these two do not completely agree on the beam spot position. for this telescope, the position of the beam spot in U1 is used for both of them with reference to their alignment with each other.

In the preceding analysis it is assumed that the source is a single point in the carbon foil. This is not physically correct but not vitally wrong in practise either. If the z_0 distance

Detector	x_0 [mm]	y_0 [mm]	z_0 [mm]
U1	-0.796	-0.676	46.76
U3	-0.600	0.502	41.27
U4	0.949	-1.182	41.40
U5	-1.513	-0.015	34.00
U6	2.200	1.094	39.24

Table 3.3: Results of the geometry calibration are inherited from Morten V. Lund [13]. z_0 is the distance from the geometric center of the detector to target. (x_0, y_0) is the distance from the geometric center to the intensity center on the detector.

between the carbon foil and the detector was included in a fit, the finite size of the source would give rise to a blur in the beam spot position, but as it is not necessary to include this distance to obtain sufficient accuracy the error in assuming a point source is negligible.

3.5.2. ENERGY CALIBRATION

Originally, the intention was for me to merely check the calibrations by Morten V. Lund from the ^{20}Mg experiment [13]. During this process some enhancements were made in the calibrations of some of the detectors. This section provides insight into the earlier and renewed calibrations.

The new energy calibrations were carried out using the Calibrator from the AUSAlib library. The Calibrator has a peak finding algorithm and takes input options on exclusion-width, oversampling and low-threshold in addition to information on target, setup and detector. With this, the Calibrator generates fits to selected peaks like the example with detector U3 in figure 3.11. Here, the low-threshold at channel number 300 ensures that most of the noise is excluded from influencing the peak finding and the exclusion-width of 120 channels is small enough for the correct peaks to be found. The oversampling makes it possible to find a peak even though it is not one of the three most intense peaks in the spectrum but it is not relevant here because of the low-threshold excluding most of noise.

When making the calibrations, it is important to incorporate the energy losses described in section 3.3. The data files store information on where the segmented detectors registered activity and this is used to calculate the angle of the particle through the dead layer and the carbon foil. Omitting this would result in a smearing out of the peaks in the spectra and blur the calibrations unnecessary.

I have used the old calibrations by Morten V. Lund for detectors U1, U2, U4 and P2. U1 is part of a telescope with the thin U2 detector and thus the energy resolution is poor for this telescope and an improvement of the calibration of this detector will hardly be noticed. The old U1 calibration was performed with β-delayed protons form the decay of ^{21}Mg. P2 is placed behind U6 and since U6 is $300\,\mu$m few dominant proton peaks from ^{21}Mg will penetrate through to P2. Instead P2 was calibrated with the α-particle source (^{148}Gd, ^{239}Pu, ^{241}Am, ^{244}Cm) with U6 removed. U2 and U4 ($20\,\mu$m and $40\,\mu$m) are too thin to stop the suitable proton calibration peaks from ^{21}Na, therefore, the calibrations of these
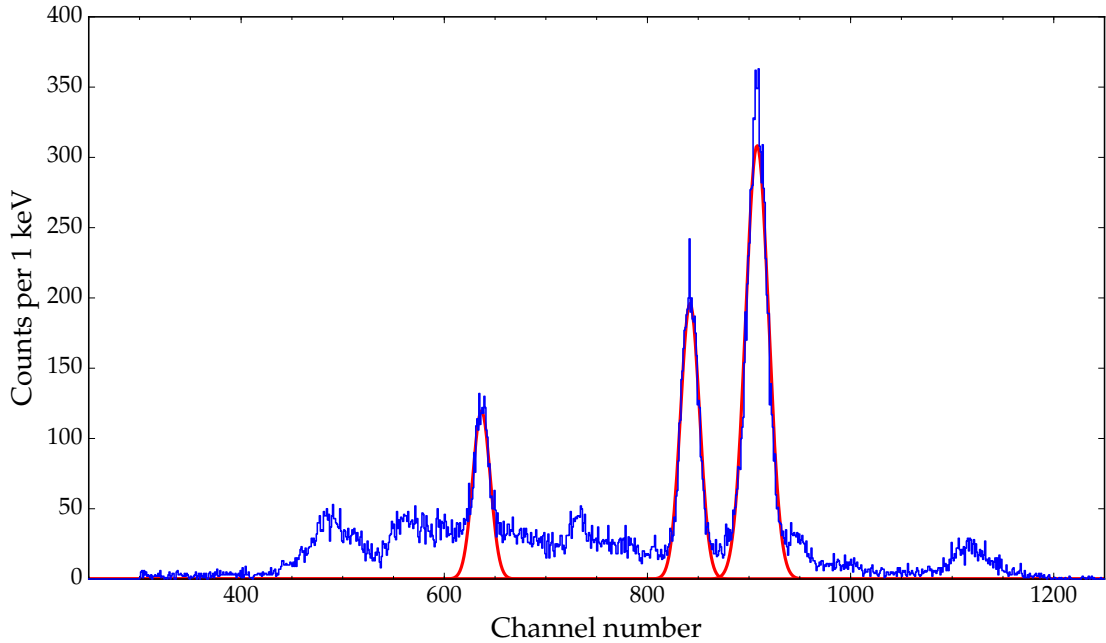
Figure 3.11: Example of a calibration spectrum. The peak finding algorithm locates the three most intense peaks in the spectrum of front strip 12 in detector U3.

two detectors were performed with β-delayed α-particles from the decay of ^{20}Na. For α calibrations it is important to remember that α-particles and protons are different particles an hence have different stopping and ionisation properties. This means that an α-particle and a proton with the same energy will not deposit the same amount of energy in the detector. Since the aim is to measure proton energies in this study the α calibrations thus need to be adjusted. The conversion factor from the energy E_α revealed by the calibration to the energy E_p I shall use is from [12]:

$$E_p = (E_\alpha - 8\,\text{keV}) \cdot \frac{\varepsilon_p}{\varepsilon_\alpha} \qquad \text{with } \frac{\varepsilon_p}{\varepsilon_\alpha} = 0.986(2)\,. \tag{3.5}$$

The $8\,\text{keV}$ appearing in the formula describes the difference in non-ionising energy loss between an α-particle and a proton and ε_x is the required energy by a particle of type x to make an electron-hole pair - corresponding to a signal in the detector. All quantities are from [12].

For the remaining DSSSDs; U3, U5 and U6, I use my new calibrations. For U3 of $60\,\mu$m the β-delayed proton branches from ^{21}Mg with laboratory energies $1252(9)\,\text{keV}$, $1773.9(6)\,\text{keV}$ and $1939.3(7)\,\text{keV}$ were used. These are calculated based on known energies from Brookhaven National Laboratory [17]. The mentioned proton branches are called p_6, p_{10} and p_{11} in the study by Morten V. Lund [13] and I adopt this notation for simplicity. p_6 is the decay branch from the $5380(9)\,\text{keV}$ level in ^{21}Na to the $1633.674(15)\,\text{keV}$ level in ^{20}Ne. Because of the poor precision on the level in ^{21}Na, p_6 is actually not most suited as a calibration peak. However, the best alternative p_8 of $1502.7(19)\,\text{keV}$ located approximately at channel number 730 in figure 3.11 does not contain enough counts to contribute to a
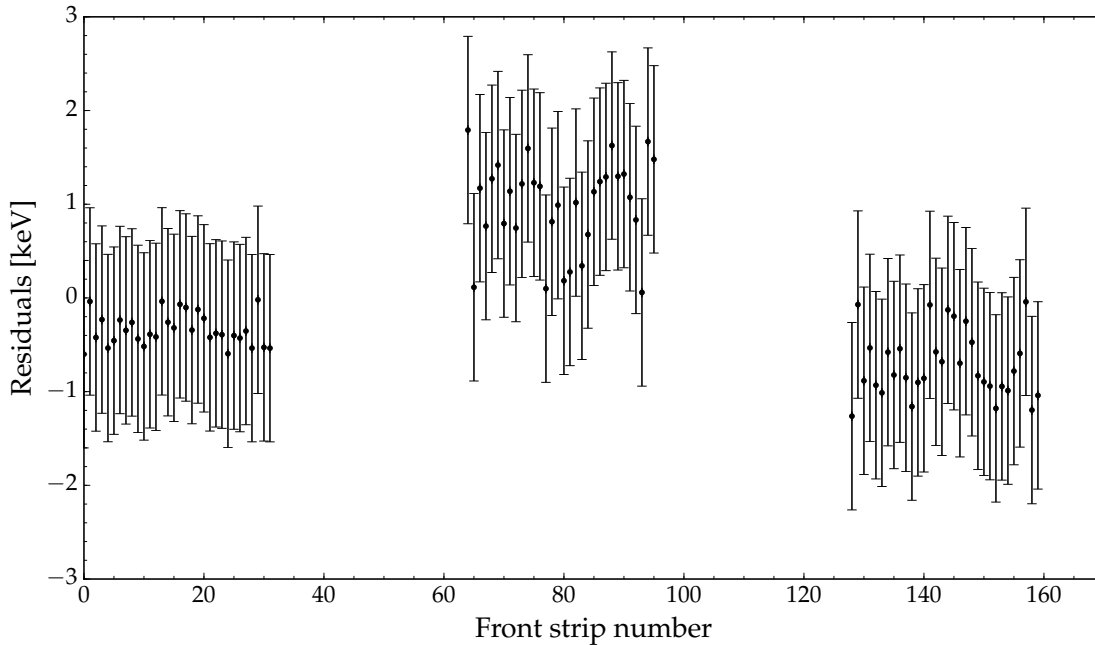
Figure 3.12: Residuals from fits to p_6, p_{10} and p_{11} in the calibration of each strip of U3. The residuals are from the fits shown in figure 3.11. The front strips in this figure are placed in the right order but on a random axis.

reliable calibration and thus p_6 is used. Making the fits in the calibration of U3 as shown in figure 3.11 reveals residuals on the position of the peaks and these are shown in figure 3.12. This plot shows an internal conformity that is almost too good to be true with the described calibration peaks. Here it is important to remember that there is a systematic error in the placement of p_6 due to the poor precision. This means that p_6 can be placed too well within its uncertainties and thus reveal a suspiciously precise energy scale. As a consequence the assessed precision on the absolute energy scale in U3 varies over the detector. Since p_6 is far from p_{10} and p_{11} compared to their separation, the precision on p_6 will affect the precision of the calibration significantly away from peaks p_{10} and p_{11}. Hence the precision for energies located between p_{10} and p_{11} is approximately 2 keV from the fit residuals visualised in figure 3.12 but only 5 keV-10 keV further from p_{10} and p_{11} where p_6 has a big influence on the calibration. With a better determined energy for the p_6 decay branch from the literature, however, there would be sufficient statistical material here to make a calibration with a precision of roughly 2 keV which would be sufficient to improve the determination of several energy levels in ^{21}Na.

The 1000 μm detector U5 is like U3 calibrated with β-delayed proton branches from ^{21}Mg; these are the peaks p_{10}, p_{11} and p_{22} with laboratory energies 1773.9(6) keV, 1939.3(7) keV and 4676.8(19) keV. These proton peaks have good precision and span a large energy range which make them suitable for a good calibration. U6 of 300 μm is also a thick detector and a good outcome would be expected with the same calibration peaks as for U5. However, U6 shows an odd energy scale for energies $\gtrsim$ 3000 keV for reasons that have not been uncovered
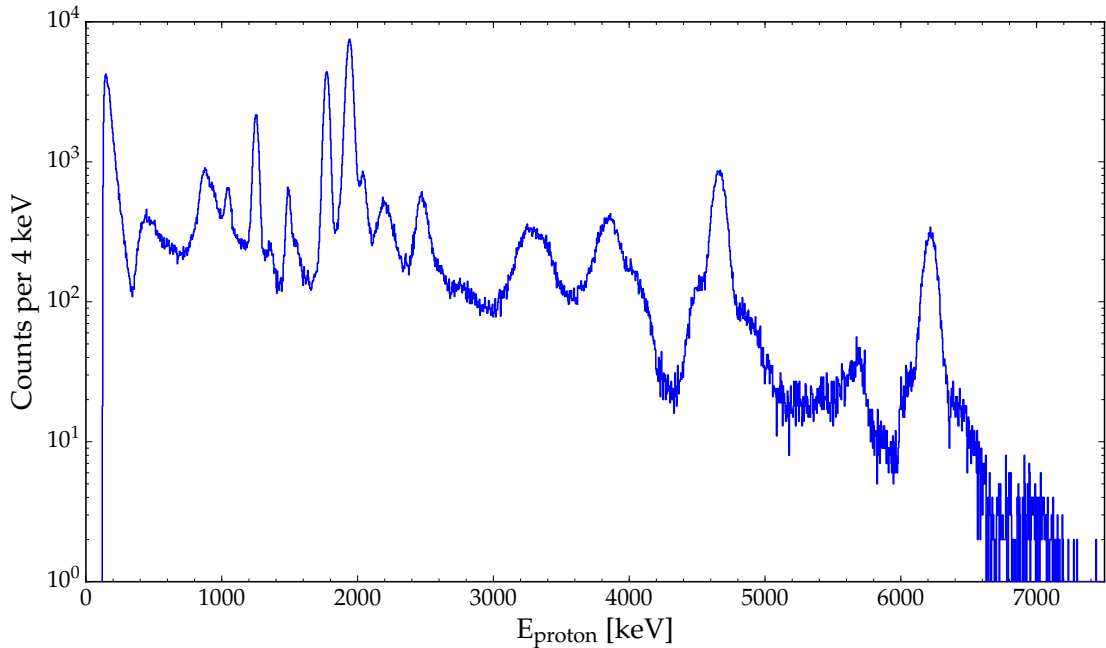
Figure 3.13: Combined spectrum of the front and rear detectors in the U3-P3 telescope. U3 stops particles with energies up to 2321 keV - above that energy data are the sum of energy deposited in both detectors as the particles penetrate U3 and stop in P3.

in this nor the previous study by Morten V. Lund. Hence for the calibration I used p_6, p_{10} and p_{11} which lie in the reliable energy range in U6. This results in a calibration where the upper energy region should be handled with care but not disregarded as the structure can still confirm result seen in the U5 detector.

To determine which calibration - old or new - to use for the remaining two pad detectors P1 and P3 I check which calibration result gives the best effective energy resolution. The quality of the calibration limits the quality of the energy resolution and measuring the width of a peak which should be narrow thus reveals the effective energy resolution. Due to the placing of the pad detectors as the back part of telescopes in the experimental setup it only makes sense to consider the energy resolution of the combined telescope and not of the pad detector by itself. To do this, I plot the combined spectra for the U3-P3 and the U4-P1 telescopes by adding the energy deposited in the front detector and deadlayers to the energy recorded in a hit in the pad detector if the event includes such a hit. The result for the U3-P3 telescope in shows in figure 3.13. The new pad calibrations were made from hits belonging to proton peaks p_{22} and p_{27} hitting the segmented front detectors in three selected pixels. Peaks p_{22} and p_{27} were chosen because their energies of 4676.8(19) keV and 6232.7(19) keV are sufficient to penetrate the front detectors in the telescopes (see table 3.1). This method for generating calibration spectra is reasonable, but unfortunately the amount of statistics here limited the quality of the calibration spectra. Hence the old calibrations exhibit the best line shapes and is thus used in this study. A summary of which calibrations are used for which detectors is gathered in table 3.4.

Detector	Old calibration	New calibration	Source
U1	x		protons from ^{21}Na
U2	x		α-particles from ^{20}Na
U3		x	protons from ^{21}Na
U4	x		α-particles from ^{20}Na
U5		x	protons from ^{21}Na
U6		x	protons from ^{21}Na
P1	x		protons from ^{21}Na
P2	x		α from (^{148}Gd, ^{239}Pu, ^{241}Am, ^{244}Cm)
P3	x		protons from ^{21}Na

Table 3.4: Summary of where the respective calibrations are from.

Detector	Thickness [μm]	σ [keV][a]
U2	20	44 (4)
U3	60	19.2 (2)
U4	40	19.9 (9)
U5	1000	13.9 (2)
U3+P3		45 (2)
U4+P1		28 (3)

Table 3.5: Energy resolutions for the relevant detectors and detector configurations.

[a]Energy resolutions for the DSSSD's are inherited from Morten V. Lund [13]. The effective resolutions of the combined telescopes are from my fits.

Generally, the energy resolution is better for thick detectors with small areas because of less noise. The detectors utilized in this experiment have approximately the same big surface area but varying thickness. The relevant energy resolutions for the different detectors are displayed in table 3.5. The resolutions for the single DSSSDs are inherited from previous studies [13] and the resolutions for the telescope configurations are assessed from the combined spectra - which figure 3.13 is an example of. This is done by fitting a normalised Gaussian to p_{27} at 6232.7(19) keV and reading out the σ-value. I have omitted the energy resolution for the U6 detector, since working with the data from this detector showed the energy scale to be untrustworthy. The poor energy resolution of detector U2 limits the expectations to the U2-U1 telescope and as the U2 detector moreover shows signs of an uneven thickness the resolution of the U2-U1 telescope will be too bad for actual use. The resolution of $\sigma = 45(2)$ keV for the combined U3-P3 telescope is significantly worse than that for the U4-P1 telescope. This was not expected and must be a result of a non-optimal calibration - even if I choose the better one. I am aware that this is a limitation but in this study, the calibrations were not meant to be a too time consuming element and thus an improvement is instead a possible task for a future project.

3.6.   CALIBRATION OF THE HPGe-DETECTORS

The aim of this study is to evaluate the decay scheme from previous studies. As a coincidence analysis between γ-rays and protons provide valuable insight the γ-spectra are of great interest and a reliable energy calibration is necessary. To test the previously determined relative intensities of the proton peaks a good efficiency calibration will be needed as well.

The HPGe detector calibrations are inherited without alterations from the previous study by Morten V. Lund [13] and the following section serves as an outline of how the calibrations were made.

ENERGY

The Clover detectors are segmented in a clover-like configuration, hence like for the segmented silicon detectors the four different germanium crystals in each of the four HPGe detectors should be calibrated separately. This was done with several intense lines from ^{152}Eu. The energy of these lines are 344.2785(12) keV, 778.9040(18) keV, 964.079(18) keV, 1085.869(24) keV, 1112.074(4) keV and 1408.006(3) keV. These calibration lines, unfortunately, lies at energies lower than those I work with in the ^{21}Mg decay as they where chosen to suit the ^{20}Mg part of the experiment.

Since data should be suitable for coincidence analysis with the silicon detectors, the same data acquisition system is used. This limits the energy resolution of the γ-spectra to approximately 5 keV. This is a worse resolution than could have been obtained for the HPGe detectors with a separate data acquisition system and is caused by a longer shaping time for the silicon detectors due to slower signal transport.

EFFICIENCY

The absolute efficiency of the detector is the number of measured photons at a specific energy compared to the total number of emitted photons at the same energy. The absolute efficiency unlike the intrinsic efficiency of the detector thus depends on the setup as scattering and attenuation of the photons can possibly influence the amount of detected photons and their energy.

The efficiency calibration is like the energy calibration made with intense lines from ^{152}Eu. ^{152}Eu provides lines with a lot of statistic over an energy range of approximately 1200 keV but the lines are still located at lower energies than the ones of interest in this study. Thus, I will rely on an extrapolation of the efficiency calibration fit.

For an efficiency calibration it is important to know the amount of decays from the source during the measurement and this can be calculated from the standard exponential decay law;

$$\text{number of decays} = N(t) - N(t + \Delta t) = N_0 \left(1 - e^{-\lambda \cdot \Delta t} \right) . \qquad (3.6)$$

Here λ is the decay constant, Δt is the measurement time and N_0 is the number of nuclei at the beginning of the measurement. N_0 is determined from the activity of the source at the time of the measurement and this in turn is calculated using the standard exponential decay law on the activity measured by the CERN Radioactivity Protection group at a
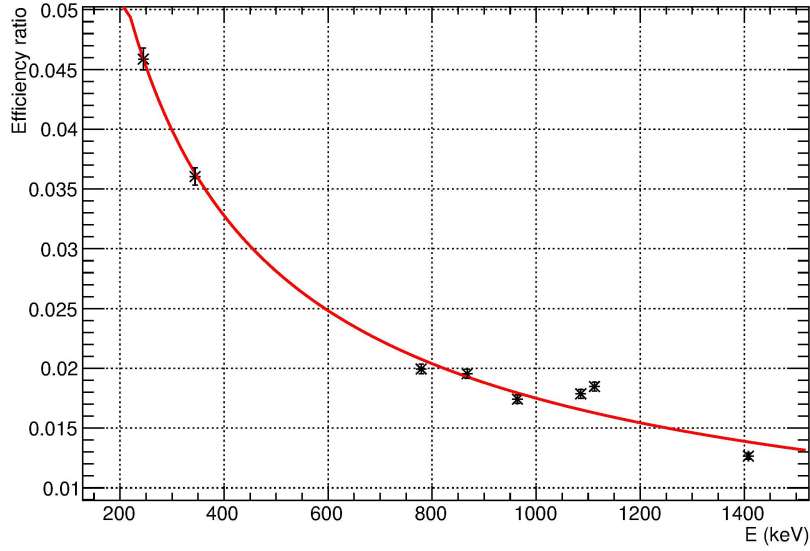
Figure 3.14: Absolute γ efficiency curve from [13].

specific time prior to the experiment. The absolute efficiency at the photon energy E_i is the dimensionless quantity

$$\varepsilon\left(E_i\right) = \left(\frac{\text{number of counts in the detector}}{\text{total number of decays}}\right)\left(\frac{I_{\gamma_i}}{100}\right)^{-1} , \tag{3.7}$$

where I_{γ_i} is the γ intensity corresponding to the calibration peak at energy E_i. The measured absolute efficiencies for the lines from the calibration source ^{152}Eu are plotted as data points in figure 3.14 and fitted by a function of the following form;

$$\varepsilon(E) = e^{p_0 + p_1 \cdot \ln(E)} . \tag{3.8}$$

Such a fit reveals the parameter values

$$p_0 = 0.869(81) \tag{3.9}$$
$$p_1 = -0.717(12) . \tag{3.10}$$

With equations (3.8)-(3.10) the absolute γ efficiency is calculated for relevant photon energies for use in the coincidence analysis in section 4.4.

Experimental findings

The overall aim of this study is to arrive at a decay scheme using the advanced coincidence analysis between photons and protons. This is then compared to previous results to determine the validity of the previous results.

In section 4.1 the data is presented in proton and γ spectra separately. Some introductory key-observations are outlined and the background is explained. In section 4.2 the half-life of ^{21}Mg is determined and the method is described. The half-life determination is a result from this study which has a slightly better precision than the previous result [14] due to more statistics. Section 4.3 presents the advantages of the telescope setup of the silicon detectors. In section 4.4 the γ coincidence analysis is discussed and in section refsec:decayscheme the results of the analysis is presented in tables showing the decay scheme and the relative intensities of the peaks.
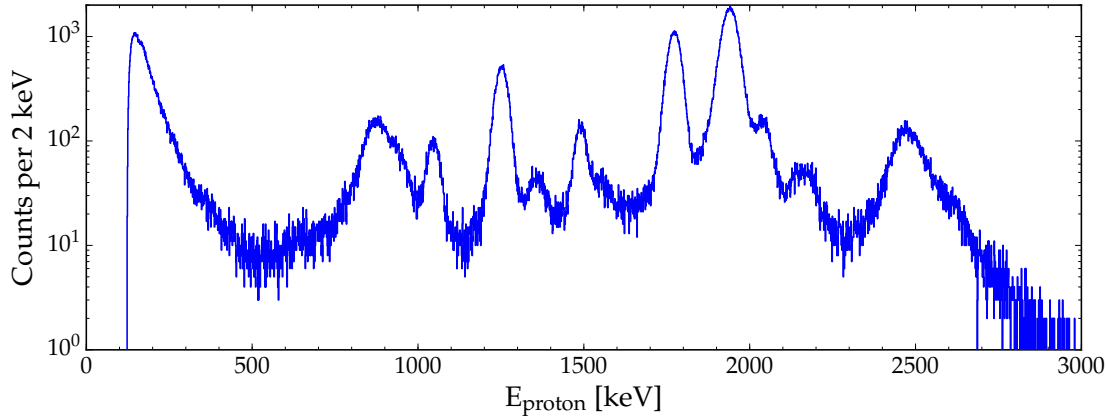
4.1. A first look at data

Often, it can be instructive to take a look at the data with an open mind before going too deep into the analysis. This section serves this purpose.
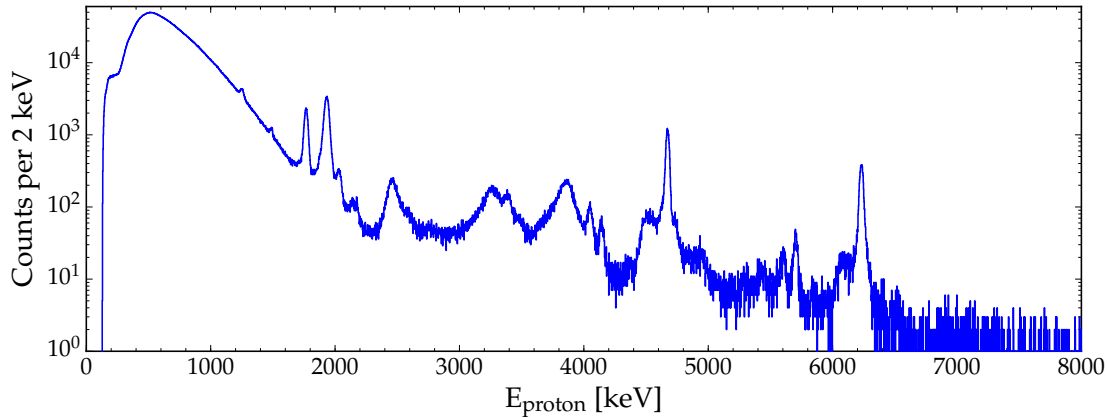
4.1.1. Proton spectra

The proton single spectra are generated from data by applying corrections for the energy lost by the protons in dead layer material and target material. The energy loss is calculated with the online calculator [8] as described in section 3.3.2 for each individual segment of the strip detectors. The resulting spectra are shown in figure 4.1 for the $60\,\mu$m silicon detector, U3, and the $1000\,\mu$m silicon detector, U5.

The proton single spectra show all the hits caught in the silicon detectors. This means that the proton spectra do not only contain proton data but also a large component of positrons from the β decay of ^{21}Mg and ^{21}Na as well as background from ion and the surroundings. According to [13] α-particles contribute a negligible amount and shall not be regarded in this analysis. As the spectra serves the purpose of revealing proton energies they shall still be called proton spectra in spite of the positrons. Nevertheless, the β-particles gives a considerable background and a task is thus to circumvent this when analysing data.

(a) The 60 μm silicon detector U3.

(b) The 1000 μm silicon detector U5.

Figure 4.1: Proton single spectra with proton energies including a correction for the traversing of dead layer and target. Note the different energy scales on the axis - the most intense peaks from the upper figure can be found in the lower as well.

The isobaric mass difference between ^{21}Mg and ^{21}Na according to [13] is 13.098(16) MeV which from equation (2.2) gives the available β decay Q-value for the β^+ decay to the ground state in ^{21}Na; $Q_{\beta+} = 12.076(16)$ MeV. This energy is of course less if the β decay goes to an excited state in ^{21}Na. The amount of energy deposited in the detectors naturally depends on the thickness of the detector and this is clear from figures 4.1a and 4.1b. Hence the different detectors have different advantages; thick detectors like U5 show a spectrum to high energies, whereas peaks at low energies only are visible in the thin detectors.

The background in the spectra does not only consist of β particles. Especially for the thin detectors (U2, U3, U4) there will be some "false" events from protons with sufficient energy to punch trough the detector. I shall look more into these events in section 4.3.

In section 2.2 the Coulomb barrier was calculated $V = 3.8$ MeV and from the sectra in figure 4.1 we see as predicted that the peaks are broader approximately at this energy and above. This is due to a higher transition rate when the Q-value is sufficiently large to
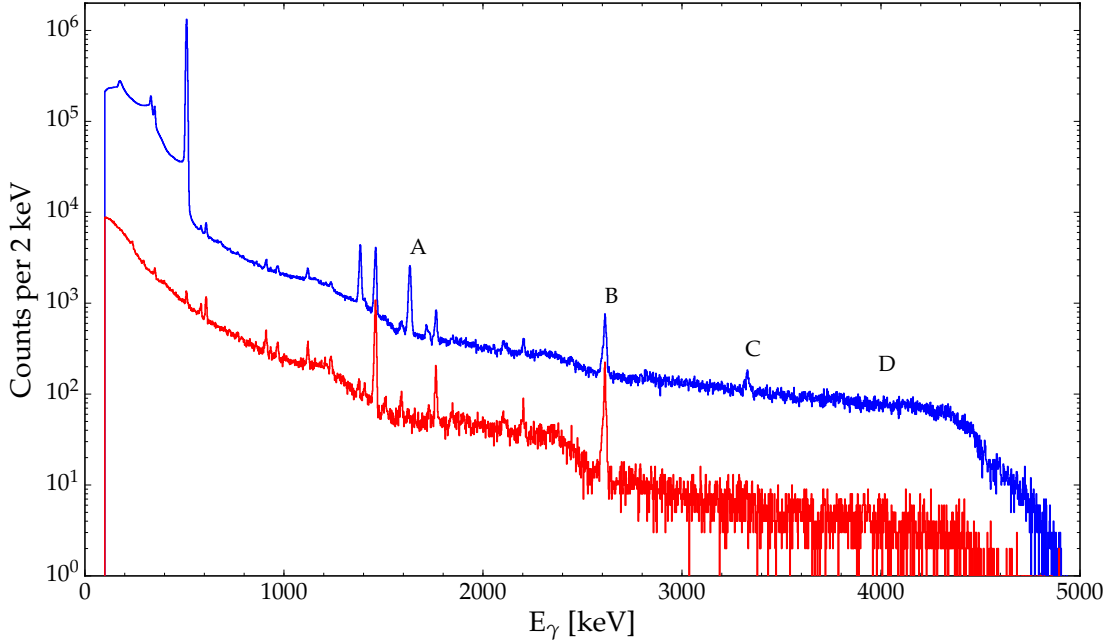
Figure 4.2: The figure shows a γ spectrum. *Blue*: spectrum obtained during the experiment. *Red*: spectrum obtained with the beam turned off. The letters A, B, C and D indicate the positions of the peaks corresponding to transitions between the lowest-lying levels in ^{20}Ne.

overcome the Coulomb barrier. As mentioned in section 2.2 the angular momentum barrier may also contribute to the energy barrier for nucleons bound in a d-wave configuration and this results in some of the relatively narrow peaks we see at energies above 3.8 MeV - for example at 5681(14) keV. The very narrow peaks at 4676.8(19) keV and 6232.7(19) keV are proton resonances from the IAS in ^{21}Na which are suppressed by isospin. The isospin of the IAS in ^{21}Na is $T = \frac{3}{2}$ whereas the proton have isospin $T = \frac{1}{2}$. These isospins can not couple to give the isospin of the low-lying levels in ^{20}Ne which have $T = 0$. As isospin needs to be conserved, these proton resonances are thus forbidden. Still we observe peaks at energies corresponding to the forbidden proton resonances from the IAS. This must be caused by mixing of the IAS with another level in ^{21}Na with a very small energy difference to the IAS. This mixing ensures that the proton emission can proceed through the admixed component with another isospin value. Thus we see the proton resonances at 4676.8(19) keV and 6232.7(19) keV in figure 4.1b and they are narrow because of the low decay rate.

4.1.2. γ SPECTRA

The HPGe Clover detectors catch the photons released in the combined reaction. In figure 4.2 the γ spectrum in shown in blue and compared to a background spectrum in red measured with the beam turned off. Due to difference in exposure time the background spectrum can not be subtracted but a comparison as shown in figure 4.2 reveals which peaks should be attributed to the background. We see here a lot of different background components. One of the prominent peaks in the background is the peak at approximately

1460 keV from β decay of ^{40}K to ^{40}Ar and subsequent photon emission. This is a photon line which is almost always present as ^{40}K is found both in humans, cement and supernovae. The 511 keV line in the γ spectrum is also considered background though not as prominent in the red background spectrum in figure 4.2. The 511 keV line comes from annihilation radiation. In general the β decay of ^{21}Mg result in several γ peaks corresponding to transitions in both ^{21}Na and ^{20}Ne. The photon peaks which connect the lowest-lying levels in ^{20}Ne and thus will be important in this study are labelled with the letters A, B, C and D in figure 4.2 and their energies are 1633.602(15) keV, 2613.8(11) keV, 3332.54(20) keV and 3987.3(17) keV respectively. The levels in ^{20}Ne which are connected by photons of these energies are shown in figure 1.2.

4.2. HALF-LIFE DETERMINATION

The first result in this study is a determination of the half-life of ^{21}Mg. To determine this value we need to consider the time distribution of the ^{21}Mg decay. This is done based on the TPROTONS data branch which stores times for all hits in the silicon detectors. ^{21}Mg is produced at the first beam production target in the setup (see section 3.1) when a beam of protons from the PSB is hitting the production target. This beam is pulsed with a bunch every 1200 ms. The pulses from the PSB are distributed between ISOLDE and the PS and hence sometime it will take multiple pulse-times between implantation of a new proton bunch on the production target. Every time a new proton bunch is implanted on target, the time is reset to zero and this causes the discontinuities in the ^{21}Mg spectrum in figure 4.3. A bunch has a length of 300 ms which can be perceived as a charging time - after that no new ^{21}Mg nuclei are produced and we observe purely decay of the ^{21}Mg nuclei. The discontinuity at approximately 370 ms was not expected. Maybe it is a component of ions from the produced beam which is blocked after the 370 ms, but even Morten V. Lund who carried out the experiment has no better explanation for this discontinuity than "it looks weird".

The TPROTONS data from the telescope front detectors U2, U3, U4, U6 with the β energy range excluded is plotted in blue in figure 4.4. This plot shows the exponential decay in activity which signifies the exponentially decreasing amount of ^{21}Mg. This tendency is fitted by the red curve in figure 4.4 with the exponential decay formula;

$$N(t) = N_0 \, e^{-\lambda t} + C \, , \tag{4.1}$$

with $N(t)$ the number of ^{21}Mg at time t, N_0 the corresponding initial number, λ the decay rate and C a constant. The constant is added to account for the small linear background and prevent it from influencing the fit. In figure 4.4 we see a slight bump a few milliseconds before the 1200 ms discontinuity. When the proton beam is implanted on target it induces a dramatic potential difference almost equivalent to a lightning bolt. To prevent this the voltage is lowered just before the gate opens to the proton beam and then raised again. The protons are only registered in detectors when the voltage is up again and thus there are a few millisecond with protons on target before they are extracted into the detectors. During this time the temperature increases rapidly and the neutrons start to evaporate. The bump
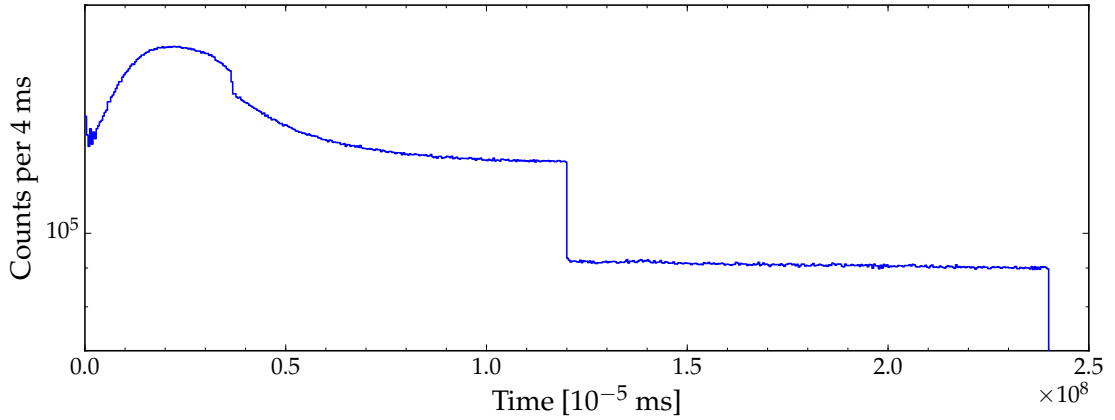
Figure 4.3: Spectrum of ^{21}Mg nuclei after production. The discontinuities every 1200 ms are due to possible reset of the time when a proton bunch hits target.
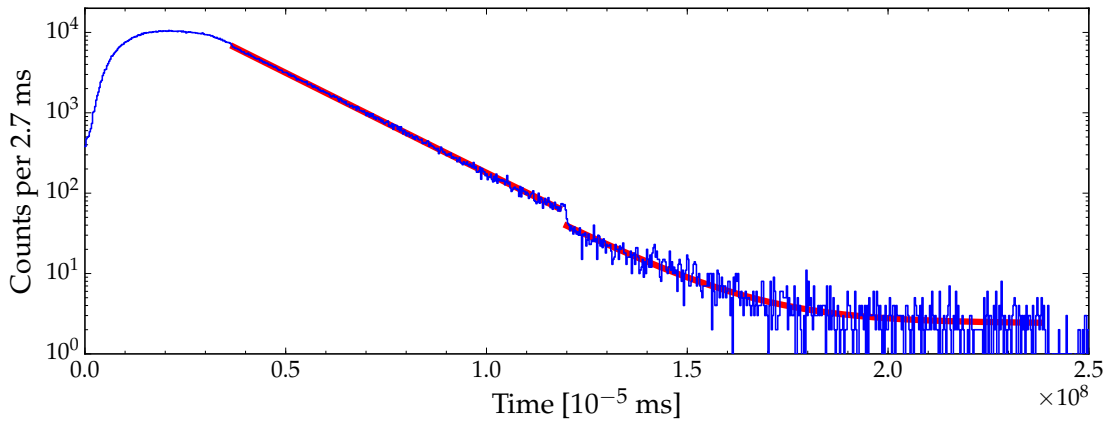

Figure 4.4: *Blue*: TPROTONS for hits in the telescope front detectors U2, U3, U4 and U6 with a proton gate. *Red*: exponential fits of the form in equation (4.1) with different values for N_0.

is hence caused by neutron reactions in the detectors. Since the neutron reactions are of no interest, the bump region is omitted from the half-life fit. With all of the unwanted regions excluded the graph is fitted in the ranges $[370\,\mathrm{ms} - 1180\,\mathrm{ms}]$ and $[1200\,\mathrm{ms} - 2380\,\mathrm{ms}]$. Allowing the parameter N_0 in equation (4.1) to vary, a value for the decay rate λ is obtained and this is converted to a half-life by the usual formula; $t_{1/2} = \ln(2)\,\lambda^{-1}$. The new value for the half-life is

$$t_{1/2} = 120.5(3)\,\mathrm{ms} . \tag{4.2}$$

The fit is made on a spectrum with more narrow bins because expanding the bins removes information. In the fit with 0.27 ms per bin the goodness of fit measured by χ^2 divided by the number of degrees of freedom (ndf) is

$$\frac{\chi^2}{\mathrm{ndf}} = 0.804 . \tag{4.3}$$

Normally, χ^2/ndf is one for a perfect fit and higher for a poor fit and thus this fit looks

artificially fine because $\chi^2/\text{ndf} < 1$. However, the article by U. C. Bergmann and K. Riisager [3] reveals that the optimal χ^2/ndf behaves differently for low count numbers. Hence, actually, the value in equation (4.3) is not suspiciously low but instead signifies a good fit. Still, there are some possible systematic uncertainties which could influence the spectrum. One of these is the 220 V connection which could give some unwanted spikes. Other components like lasers and other equipment in the area could also induce a background. Looking at the spectrum in figure 4.4 there might be some systematic structure around 1000 ms. It would be unfortunate if the systematic uncertainties are influencing the spectrum around the top at ≈ 400 ms or in the tale at $[1400\,\text{ms} - 1600\,\text{ms}]$ as the fit is more sensitive to uncertainties in the edges. In this case the half-life might be affected, hence I made the conservative choice of adding 0.1 ms to the uncertainty resulting around the result in equation (4.2).

4.3. Utilizing the telescope set-up

The telescope setup described in section 3.2 has several advantages. When particles punch through a thin front detector and is stopped in the back, for example, it is possible to determine the type of particle based on the amount of energy it lost in the front detector. This and other techniques enabled by the telescope configurations is outlines below.

Back anti-coincidence

When a particle has sufficient energy to punch through the front detector it will deposit some energy in the detector which is not its full energy. This will blur the spectrum and hide the information from the particles that are stopped completely in the detector. An example of this is shown with the red spectrum in figure 4.5 for the $40\,\mu$m silicon detector U4. Making an anti-coincidence gate with the back detector in the telescope all the particles which are detected in coincidence with a hit in the back detector - P1 in this case - are excluded. This excludes some good low-energy proton events in random coincidence with a β but this is a minor component and the spectrum is much more clear. The blue spectrum in figure 4.5 shows the back anti-coincidence spectrum for U4. The back anti-coincidence gate is only applied to the thin detectors U2 and U4. Application of a gate alters the data and the gain has to be visible on order to justify making the gate. The thinnest detectors experience the most punch through protons and the benefit of the back anti-coincidence is clear here.

Combined front-back spectrum

The back detectors in the telescopes can, of course, not just be used for subtracting data. The punch through protons deposit some energy in the front detector, dead layers on front and back of the front detector and front of the back detector, and target. Using the information on where in the segmented front detector the hit was recorded, the total energy loss prior to the back detector can be calculated. The lost energy is then added to the energy deposited in the back detector to reconstruct the total laboratory energy of the
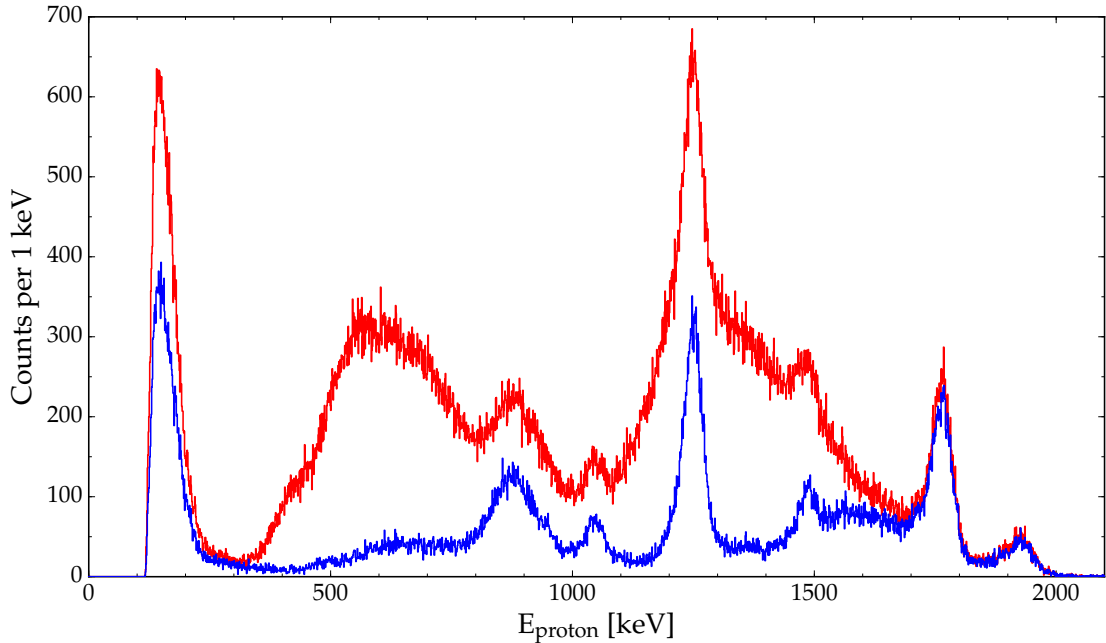
Figure 4.5: Proton single spectrum for the 40 μm detector U4. *Red*: Spectrum of all hist in U4. *Blue*: Spectrum with a back anti-coincidence gate excluding all hits in U4 which punch through to P1.

punch through proton. The energies of the punch through protons can then be filled into the same proton spectrum as the particles which stop completely in the front detector. The result is what I call a combined front-back spectrum and an example is shown in figure 4.6 for the U3-P3 telescope.

By exploiting this possibility of making a combined spectrum I have an additional spectrum that covers the same energies as the thick detectors, U6 and U5. This is a way of consolidating the results from these thick detectors. However, the energy resolution of the combined spectra limits the usability in this specific case.

dE-E SPECTRUM

In the one dimensional combined spectrum described above the energy deposited in the front and back detectors are added to a single value. If, instead, the energies deposited in the two different detectors are plotted against each other, a two dimensional so-called dE-E spectrum will emerge. In figure 4.7 a dE-E spectrum is plotted for the U4-P1 detector telescope with the constraint that there had to be exactly one hit in both front and back detector. This constraint excludes a few good events because of random coincidence with a β particle but it ensures a more reliable matching between front and back hits. The energies are modified corresponding to all particles impinging perpendicular on the detector. This is done using equations from [10] with dE' and E' being the measured energies with dead
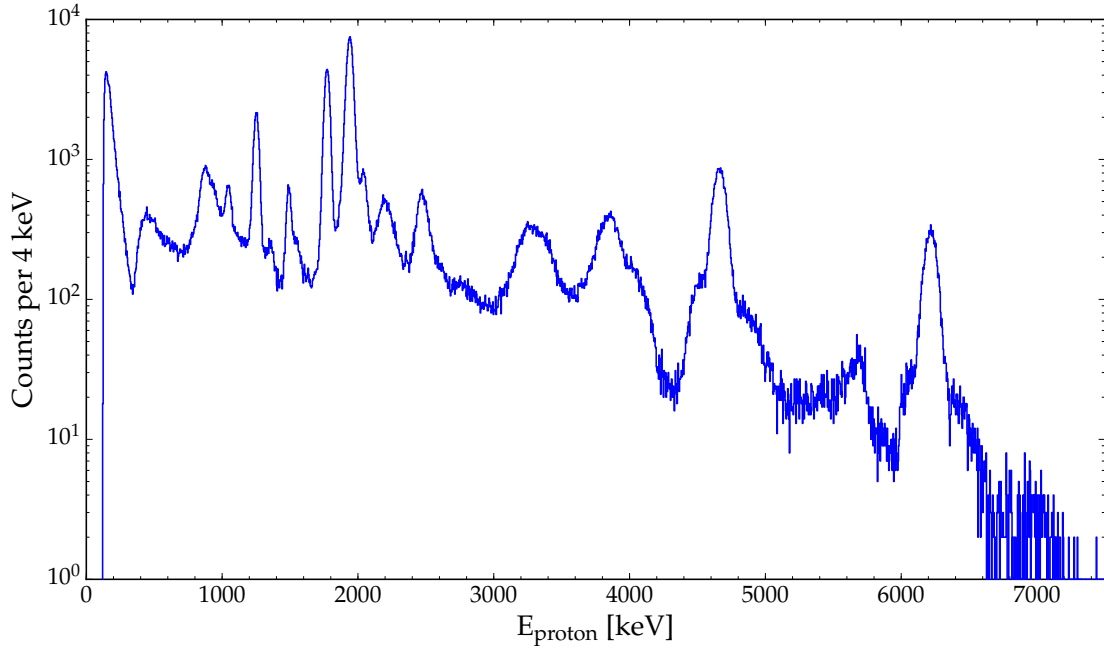
Figure 4.6: Combined front-back proton spectrum for the U3-P3 telescope. The hits which punch through the U3 detector are recorded in the P3 detector and added to the spectrum with corrected energy.
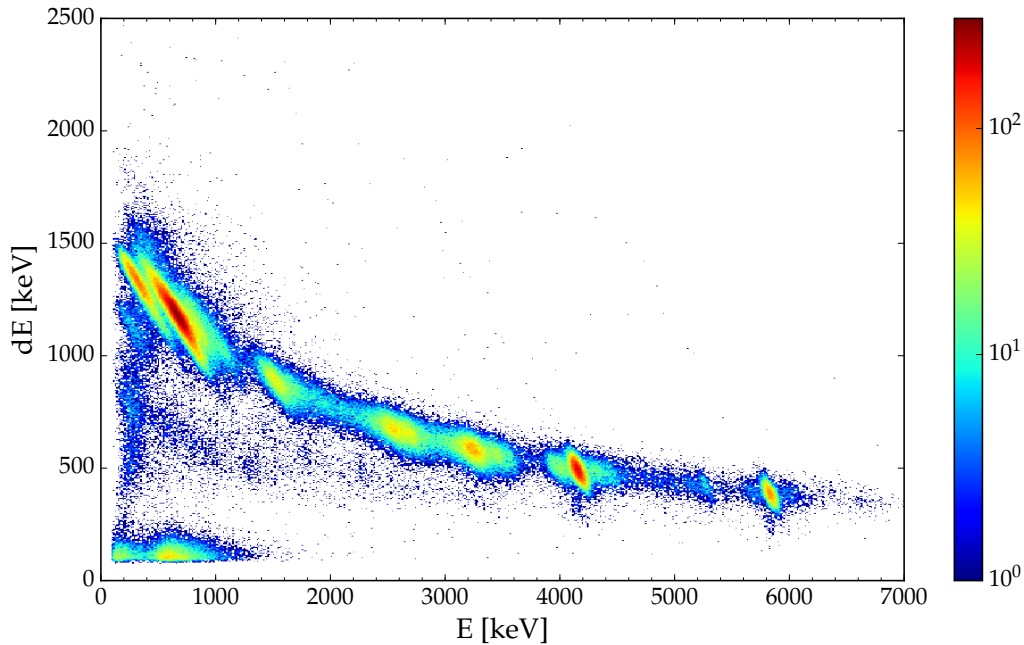
Figure 4.7: The figure shows a dE-E spectrum for the U4-P1 detector telescope. The spectrum is adjusted using equations (4.4) and (4.5) from [10]. The figure has 500×500 bins. Figures containing dE-E spectra from the remaining three telescopes can be found in appendix A.1.

layer and target corrections included;

$$dE = \cos(\theta) \, dE' \tag{4.4}$$

$$E = E' + (1 - \cos(\theta)) \, dE' \; . \tag{4.5}$$

θ is the angle between a particle track hitting perpendicularly into the detector and the actual track of the particle which determines in which segment on the detector the particle is recorded.

The plot shows a clear distinction between different types of particles, as mentioned initially. The upper banana-shaped part of the events are protons and the more intense lumps in the banana correspond to the peaks in figure 4.1. The events in the bottom of the figure correspond to all β events where the β was recorded both in the front an back detector. The more diffuse point under the banana looks like goods proton events in the front detector in random coincidence with a β in the back detector.

The blank space leftmost in figure 4.7 is caused by the ADC which only reads out data when the energy exceeds a specific limit. If this trigger of seemingly $100 \, \text{keV}$ is not activated in the back detector there is no recorded hit and hence the sharp line in the plot.

There is a division of the β lump in the bottom. The left part of the lump is from events where the β trigger a readout in the front detector and the right part would similarly correspond to the β triggering the readout in the back detector. The readout trigger threshold is not sharp like the ADC trigger threshold and this might be due to a fuzzy trigger threshold in the back detector. The particles need to have a specific energy to trigger the detector but if the threshold is fuzzy a less intense β might activate the trigger. The fuzziness of the trigger is very plausible since the readout happens very fast and a small amount of noise will have a relatively big impact in that instant. This is a contrast to the ADC trigger threshold where the readout is slow and hence the whole energy of the triggering particle spike is integrated which eliminates the influence of noise.

More dE-E spectra for the remaining telescopes can be found in appendix A.1.

4.4.   γ-COINCIDENCE ANALYSIS

The ability to make a γ-coincidence analysis is the biggest advantage in this study compared to the previous study [13]. I construct proton spectra with gates on γ energies such that protons in coincidence with a photon of the chosen energy are enhanced in the spectrum. The γ gates are constructed around the peak energies labelled in figure 4.2. Figure 1.2 visualises the proton branches to the lowest-lying excitation levels in ^{20}Ne and unless the proton branch goes to the ground state in ^{20}Ne there is a subsequent γ emission of one or more of the energies labelled in figure 4.2. Table 4.1 shows the allowed γ transitions between the lowest-lying states in ^{20}Ne with the states labelled by their energy, spin and parity. Each of the levels have one strong γ transition and the energies corresponding to those transitions are written in bold font in table 4.1. It is clear from the table, that the most intense γ transition from the second, third and fourth excitation levels all result in a second γ emission from the first excitation level to the ground state. Hence when gating on the energy corresponding to the $2^+ \rightarrow 0^+$ transition I expect to see components from

Initial state in ^{20}Ne [keV, J^π]	Final state in ^{20}Ne [keV, J^π]	E_γ [keV]	I_γ
1633.674 (15), 2^+	g.s., 0^+	**1633.602 (15)**	100
4247.7 (11), 4^+	1633.674 (15), 2^+	**2613.8 (11)**	100
4966.51 (20), 2^-	1633.674 (15), 2^+	**3332.54 (20)**	99.4 (2)
	g.s., 0^+	4965.85 (20)	0.6 (2)
5621.4 (17), 3^-	4966.51 (20), 2^-	654.9 (18)	4.8 (16)
	1633.674 (15), 2^+	**3987.3 (17)**	87.6 (10)
	g.s., 0^+	5620.6 (17)	7.6 (10)

Table 4.1: A list of the allowed γ transitions between the lowest-lying levels in ^{20}Ne labelled by their excitation energy and spin and parity [17]. g.s. is short for ground state. The intensities of the different γ decay branches from a level sum to 100. The γ energies in **bold** are center of gates on γ energies.

all the proton peaks going to the higher excitation levels in ^{20}Ne as well. In table 4.2 the laboratory energies of all the peaks are listed together with an overview of which γ peaks they are expected to be coincident with. The peak energies, E_{proton}, are calculated as

$$\frac{20}{21}\left(E_{^{21}Na} - S_p\left(^{21}Na\right) - E_{^{20}Ne}\right) \tag{4.6}$$

where $E_{^{21}Na}$ denotes the energy of the level in ^{21}Na that emits the proton, $E_{^{20}Ne}$ is the energy of the level in ^{20}Ne that receives the proton and $S_p\left(^{21}Na\right) = 2431.68(28)\,\text{keV}$[13] is the proton emission threshold in ^{21}Na. The fraction $\frac{20}{21}$ accounts for the recoil of the proton emission mother nucleus. The energies listed in table 4.2 are the energies the peaks are expected to be located at in the spectra.

Proton branches to the highest excitation levels in ^{20}Ne generally have the lowest proton energies. If a peak which was expected to go to the ground state turns out to be coincident with a γ corresponding to a high excitation level - or vice versa - the same amount of counts suddenly equals a very different decay strength. This is due to the phase space which is much larger for the lower than for the upper levels in ^{21}Mg. Thus there is most potentially new physics in the study of the proton peaks with the lowest energy.

An attempt on removing the background in the coincidence spectra was made with a time gate on the TPROTONS data branch. This gate, however, shows a reduction in good counts of the same size as the background reduction. This shows that the background counts in the coincidence spectra comes from ^{21}Mg and not from other components in the beam. Hence a time gate is not applied to the coincidence spectrum data.

Below are subsections for each of the four gates on γ energies with a description of the analysis of the coincidence spectra with each gate. The analysis includes measuring the counts associated with each coincidence peak and comparing this amount to the amount of counts in the same proton peak in the single proton spectra. Where it is possible the peak contents are measured by counting and the uncertainty is then the square root of the count. The background is counted and subtracted and the uncertainty in the background count is

| | E_{proton} [keV] | Expected in coincidence with γ with E_γ [keV] | | | |
		1633.602 (15)	2613.8 (11)	3332.54 (20)	3987.3 (17)
p_1	383.4 (7)	x			
p_2	862 (12)	x		x	
p_3	879 (3)	x		(x)	x
p_4	885 (14)	x	x		
p_5	1059.6 (5)				
p_6	1252 (9)	x			
p_7	1386 (14)	x	x		
p_8	1502.7 (19)	x		x	
p_9	1546 (12)	x	x		
p_{10}	1773.9 (6)				
p_{11}	1939.3 (7)				
p_{12}	2000 (29)	x			
p_{13}	2167 (19)	x			
p_{14}	2181 (2)	x	x		
p_{15}	2465 (9)				
p_{16}	3288 (19)				
p_{17}	3375 (14)	x			
p_{18}	3844 (19)				
p_{19}	4036 (12)	x			
p_{20}	4125 (14)	x			
p_{21}	4535 (14)	x			
p_{22}	4676.8 (19)	x			
p_{23}	4931 (14)				
p_{24}	5592 (12)				
p_{25}	5681 (14)				
p_{26}	6091 (14)				
p_{27}	6232.7 (19)				
p_{28}	6946 (23)				

Table 4.2: The energies, E_{proton}, are calculated using energies from NNDC [17] and the proton separation energy $S_p(^{21}Na)= 2431.68(28)$ keV [13].

added to give the total uncertainty. In the single spectra the peaks are fitted by normalised Gaussian functions. The line shapes of the peaks can be approximated by the normalised Gaussian but are never exactly Gaussian and thus the fitting introduces a systematic error which we need to keep in mind. Formally, the number of counts in the proton spectrum, N_p, is given by

$$N_p = N_0 \, b_{p\gamma} \, \varepsilon_p \, , \tag{4.7}$$

with N_0 the total number of decays from the level in ^{21}Na, $b_{p\gamma}$ the branching ratio of the relevant proton-γ branch and ε_p the proton efficiency of the silicon detector. Correspondingly,

E_γ [keV]	ε_γ
1633.602 (15)	0.0118 (22)
2613.8 (11)	0.0085 (16)
3332.54 (20)	0.0071 (14)
3987.3 (17)	0.0062 (12)

Table 4.3: List of γ efficiencies, ε_γ, of the HPGe detectors at the relevant γ gate energies, E_γ.

the number of counts in the coincidence spectrum, $N_{p\gamma}$ is

$$N_{p\gamma} = N_0 \, b_{p\gamma} \, \varepsilon_p \, \varepsilon_p \gamma \, , \tag{4.8}$$

where ε_γ is the γ efficiency of the HPGe detectors. The γ efficiencies are calculated for each of the four γ peak energies using equation (3.8) with the parameters form equations (3.9) and (3.10). This gives the efficiencies listed in table 4.3. Equations (4.7) and (4.8) give the expected relation between observed counts;

$$\frac{N_{p\gamma}}{N_p \, \varepsilon_\gamma} = 1 \, . \tag{4.9}$$

If this is within the uncertainties for the measured counts in the coincidence spectra compared to the single spectra the conclusion is that the peak is correctly assigned in coincidence with the γ the gate is constructed to fit.

The second part of the analysis is a determination of the realtive intensities of the peaks based on the contents in the peaks in the single spectra. The reference point is p_{11} which is assigned a relative intensity of 100. This analysis used the solid angles of each detector which can be found in table 3.1. The solid angles are important because they are not exactly the same and the peaks are not necessarily measured in the same detector.

4.4.1. GATE AROUND THE $1633.602(15)\,\text{keV}$ γ PEAK

The γ gates are constructed to wrap closely around the peaks in the γ spectrum. For the $1633.602(15)\,\text{keV}$ γ peak the gate is $[1616\,\text{keV} - 1650\,\text{keV}]$ and it is marked by a red box in figure 4.8. A background coincidence spectrum is constructed with a the γ gate $[1656\,\text{keV} - 1690\,\text{keV}]$ which is marked by a black box in figure 4.8. Corresponding figures for the γ gates on the three other γ peaks from table 4.1 are displayed as figures A.8, A.9 and A.10 in the appendix.

With the γ gate visualised in figure 4.8 the proton-γ coincidence spectra are generated. An example of such a coincidence spectrum is shown in figure 4.9 for hits in the U3 detector. The colors in the plot correspond to the colors marking the gates in figure 4.8; red is around the $1633.602(15)\,\text{keV}$ peak and black is the background. Corresponding figures from the other detectors are shown as figures A.4, A.5, A.6 and A.7 in appendix A.2.

From table 4.2 a lot of proton peaks are expected to be visible in the $1633.602(15)\,\text{keV}$ gate. They are listed below with notes on key points in the analysis

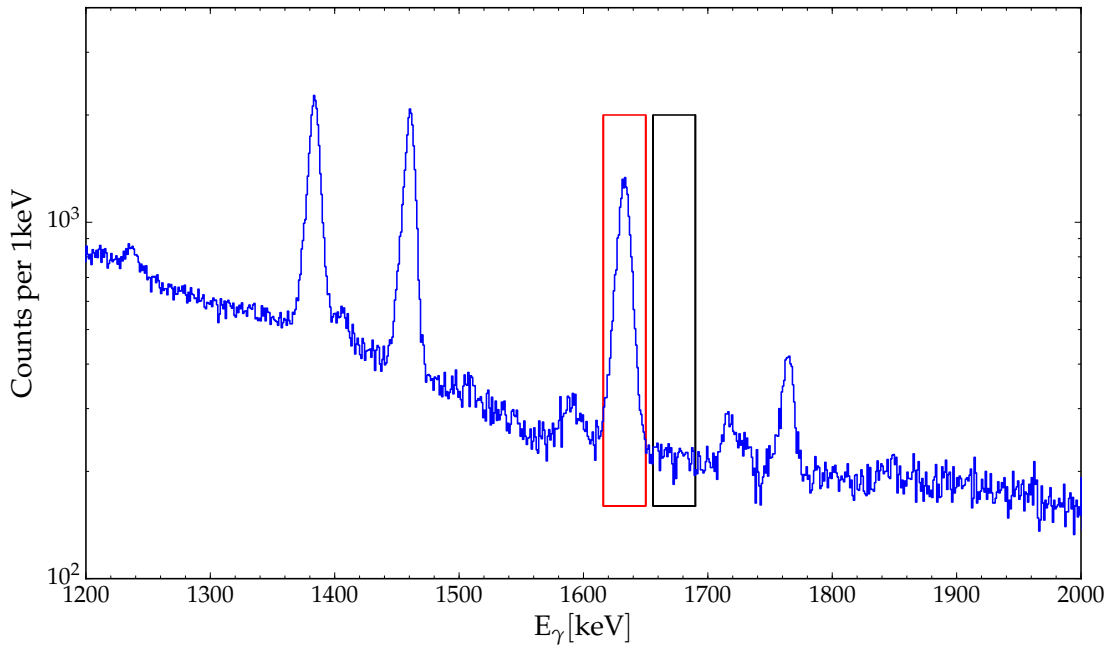**Figure 4.8:** γ spectrum with the gate on γ energies marked in red on top of the spectrum. The gate is $[1616\,\text{keV} - 1650\,\text{keV}]$. The black box marks the gate $[1656\,\text{keV} - 1690\,\text{keV}]$ used for the background coincidence spectrum.
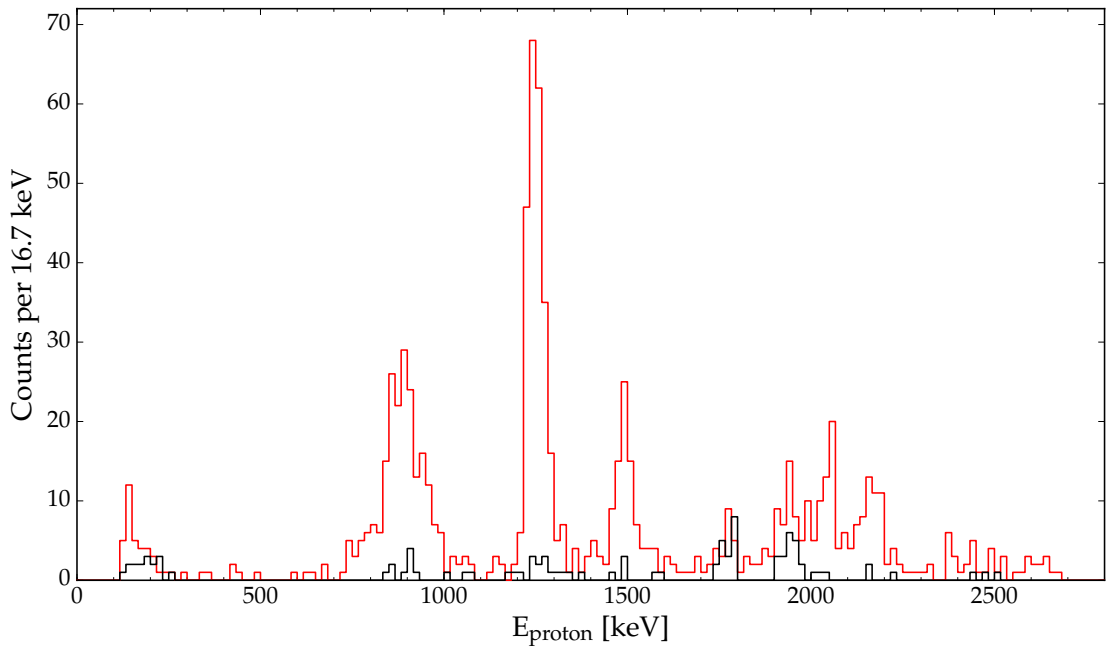

Figure 4.9: Coincidence spectrum in the U3 detector with a gate around the $1633.602(15)\,\text{keV}$ γ peak. The gate is marked in figure 4.8. The red spectrum shows the good events and the black spectrum shows the background.

p_1; $383.4(7)\,\text{keV}$: p_1 is found in the U2 detector spectrum, figure A.4. The content in the coincidence spectrum is counted manually and the content relation is

$$\frac{N_{p\gamma}}{N_p\,\varepsilon_\gamma} = 1.4(3) \; . \tag{4.10}$$

The relative intensity is multiple times higher than expected, but there are systematic tendencies in the U2 single spectrum which may account for this diversion: p_1 is located at the noise limit in the U2 spectrum and thus the noise might have contributed to what appeared to be the content of p_1. Moreover, the back anti-coincidence is not 100% safe; some of the events can scatter after going through U2 and before reaching U1. Because U2 is so thin $(20\,\mu\text{m})$ and U1 is so thick $(500\,\mu\text{m})$ approximately 100 times more events are caught in U1 relative to U2 and thus even a very small part of these events in U1 can make a big difference in U1 if the back anti-coincidence is incomplete. Hence, overall, this result is a satisfactory confirmation of the placement of p_1 in coincidence with a $1633.602(15)\,\text{keV}$ γ.

p_2 - p_3 - p_4; $862(12)\,\text{keV}$ - $879(3)\,\text{keV}$ - $885(14)\,\text{keV}$: p_2, p_3 and p_4 are spotted in detector U3 (figure 4.9) where they appear as one broad peak because they are so close in energy. I call them the low-energy triplet. The separation of these three peaks is in deed a task for the coincidence analysis with gates on the three other γ peaks. The content measurements reveal;

$$\frac{N_{p\gamma}}{N_p\,\varepsilon_\gamma} = 1.2(3) \; , \tag{4.11}$$

which is in accordance with all the three proton peaks being coincident with a $1633.602(15)\,\text{keV}$ γ.

p_6; $1252(9)\,\text{keV}$: p_6 appears in the U3 detector with a content well within the expected range;

$$\frac{N_{p\gamma}}{N_p\,\varepsilon_\gamma} = 1.1(2) \; . \tag{4.12}$$

There is thus no problems in the previous assignment of the strong p_6 proton peak in the decay scheme.

p_7; $1386(14)\,\text{keV}$: p_7 is located on the edge of the very intense p_6 peak. The content measurement for p_7 thus relies on a conservative estimate using the spectrum corresponding to the U3 detector. The upper limit on the content is estimated using the Garwood 95% confidence interval from [2]. The upper limit for the content relation is then;

$$\frac{N_{p\gamma}}{N_p\,\varepsilon_\gamma} = 1.4(3) \; , \tag{4.13}$$

and the upper limit on the counts in the coincidence peak is hence by far sufficient for the expected consistency. The relative intensity of the p_7 peak in the single spectrum, however, is approximately half of the previously determined relative intensity and well outside the uncertainties. This indicates that the estimate of the content of the p_7 peak in the single spectrum is too low. The single spectrum content can be revised upwards to within the

uncertainty of the previously determined relative intensity by reassigning some of the counts from p_6 to p_7. Doing this, the upper limit on the content of the coincidence peak relative to the single spectrum peak is only $N_{p\gamma}/(N_p\,\varepsilon_\gamma) = 0.66(4)$. This could indicate a flawed determination of the content of p_7 in the coincidence spectrum; when two peaks are as close to each other as p_6 and p_7 it can be difficult to tell their respective contents apart. p_6 has more counts than strictly needed for consistency and a reinterpretation of the affiliation of just a few counts could save p_7 in this coincidence analysis.

$\underline{p_8;\ 1502.7(19)\,\mathrm{keV}:}$ p_8 is a relatively strong peak at $1502.7(19)\,\mathrm{keV}$ in the U3 spectrum in figure 4.9. The estimate of its content gives the relative content;

$$\frac{N_{p\gamma}}{N_p\,\varepsilon_\gamma} = 1.6(4) \ . \tag{4.14}$$

This is more than expected but as outlined below the neighbouring p_9 is short on counts in the initial assessment and a different distribution of the counts in their common energy range will even out the deviations. A redistribution results in the relative content being $N_{p\gamma}/(N_p\,\varepsilon_\gamma) = 1.4(4)$, for the p_8 peak which looks more promising. The relative intensity of the p_8 peak in the single spectrum is a bit low compared to previous results. This indicates that not all of the p_8 peak is included in the fit to determine the content in the single spectrum. With a relative content value of $1.4(4)$ there is room for an upward adjustment of the peak content in the single spectrum.

$\underline{p_9;\ 1546(12)\,\mathrm{keV}:}$ p_9 in the U3 detector has as mentioned above initially been assigned a content which shows a relative content measure of

$$\frac{N_{p\gamma}}{N_p\,\varepsilon_\gamma} = 0.6(3) \ , \tag{4.15}$$

which is in the low end. The redistribution of counts mentioned above with an additional uncertainty from the reassigned counts show a relative content of the p_9 coincidence peak of $N_{p\gamma}/(N_p\,\varepsilon_\gamma) = 1.3(6)$. The uncertainty here is large because the redistribution approximately doubled the content associated with p_9 and the square root of the number of redistributed counts are added directly to the uncertainty. As for p_8 the relative intensity of p_9 is on the low side. The argumentation to account for this follows the exact same course as for p_8 above.

$\underline{p_{12};\ 2000(29)\,\mathrm{keV}:}$ p_{12} was spotted in the U3 detector and the counts attributed to p_{12} result in a relative content of

$$\frac{N_{p\gamma}}{N_p\,\varepsilon_\gamma} = 1.1(3) \ , \tag{4.16}$$

which signifies a confirmation of the previous placement of p_{12} in the decay scheme.

$\underline{p_{13}\ \text{-}\ p_{14};\ 2167(19)\,\mathrm{keV}\ \text{-}\ 2181(2)\,\mathrm{keV}:}$ p_{13} and p_{14} are both expected to be coincident with a $1633.602(15)\,\mathrm{keV}$ γ and qua their small energy difference they are inseparable in this
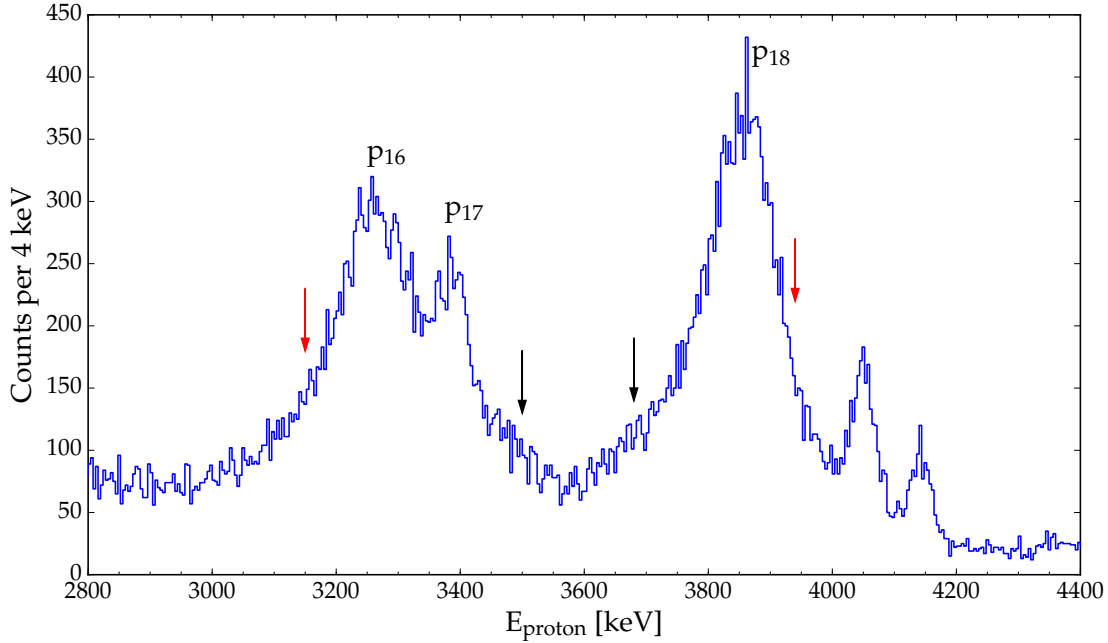
Figure 4.10: Single spectrum in detector U5. The zoom shows the area between peaks p_{17} and p_{18}. The red arrows indicate areas with destructive interference between peaks p_{16} and p_{18}; left of p_{16} and right of p_{18}. Black arrows, correspondingly, show constructive interference areas.

coincidence spectrum. Their combined content reveals the relation

$$\frac{N_{p\gamma}}{N_p\,\varepsilon_\gamma} = 1.3(3) \ . \tag{4.17}$$

The total content of p_{13} and p_{14} in the single spectrum in U3 reveals a relative intensity lower than expected form previous results. An upward adjustment corresponding to inclusion of more of what might wrongly have been interpreted as background in the single spectrum corrects the relative intensity and still keeps the content relation between the coincidence and single spectra consistent well within the uncertainties.

$\underline{p_{17};\ 3375(14)\,\text{keV}:}$ p_{17} is observed in the spectrum from the U5 detector. p_{17} is located in the slope of the more intense p_{16} and in this region the line shapes are asymmetric as shown in figure 4.10. A possible reason for this asymmetry is interference between peaks which is a known phenomenon described in [18]. This looks like an interference effect as the amplitude for the interference changes sign from one side of a peak to the other [9]. In figure 4.10 arrows point to the regions with constructive and destructive interference: Black arrows is constructive interference in the region between p_{16} and p_{18} and the red arrows indicate destructive interference in the regions beyond. In order to have interference the interfering peaks need to have the same spin of their initial states and the same final state [9]. The decay branches corresponding to p_{16} and p_{18} both end in the ground state of ^{20}Ne. The initial state of p_{18} in ^{21}Na has $J^\pi = 3/2^+$ and the initial state of p_{16} has a spin in the triplet $(3/2, 5/2, 7/2)^+$. The observed interference indicates that the spin of the

initial state of p_{16} which is the $5884(20)$ keV level in ^{21}Na really has $J^{\pi} = 3/2^{+}$.

Back to p_{17} which with a fitted measure of the content in the single spectrum peak shows an unsatisfactory

$$\frac{N_{p\gamma}}{N_p\,\varepsilon_\gamma} = 5.1(13) \ . \tag{4.18}$$

The relative intensity shows a content of p_{17} which is way too low in the single spectrum as well. Both these results would be improved if the content of p_{17} in the single spectrum turns out to be severely underestimated in this analysis. That, however, would require some additional considerations and hence this is merely identified as a problem here. The problem, nevertheless, is not solved by concluding that p_{17} is not coincident with a $1633.602(15)$ keV γ and thus p_{17} is not moved in the decay scheme based on this study.

$\underline{p_{19} - p_{20};\ 4036(12)\,\text{keV} - 4125(14)\,\text{keV}:}$ p_{19} and p_{20} are inseparable in the $1633.602(15)$ keV γ coincidence spectrum in detector U5. There is no doubt that they are two separate peaks in the single spectrum but for the coincidence analysis they are considered together. The content of the total p_{19}-p_{20} coincidence peak relative to the sum of their contents in the single spectrum is

$$\frac{N_{p\gamma}}{N_p\,\varepsilon_\gamma} = 0.6(23) \tag{4.19}$$

with background counts added to the fitted contents in the single spectrum. These fits are not too reliable as both p_{19} and p_{20} are placed on the slope of p_{18} which are interfering with p_{16} - see figure 4.10. Thus this is interpreted as a confirmation of the coincidence of p_{19} and p_{20} with a $1633.602(15)$ keV γ. The relative intensities of peaks p_{19} and p_{20} considered individually in the single spectrum from U5 are also consistent with previously determined values when the background is included.

$\underline{p_{21};\ 4535(14)\,\text{keV}:}$ p_{21} is spotted in U5 where it lies close to the very intense peak, p_{22}. Distinguishing between the contents of two closely spaced peaks is not a conclusive task, however, a reasonable distribution gives a content relation of

$$\frac{N_{p\gamma}}{N_p\,\varepsilon_\gamma} = 0.7(2) \ . \tag{4.20}$$

This is consistent with a confirmed coincidence - especially as the fits to the single spectrum are conducted with simplified Gaussian functions in stead of a formally correct R-matrix analysis which will inevitably induce some errors. The overall fit quality also excuses the relative intensity of the p_{21} peak in the single spectrum from U5 even though the relative intensity deviates with approximately 10% from the previous value.

$\underline{p_{22};\ 4676.8(19)\,\text{keV}:}$ p_{22} is located next to p_{21} in the U5 spectrum and with the distribution of counts mentioned above p_{22} reveals a relative content between coincidence spectrum and single spectrum of

$$\frac{N_{p\gamma}}{N_p\,\varepsilon_\gamma} = 0.80(18) \ . \tag{4.21}$$

This confirms the coincidence of p_{22} and the 1633.602(15) keV γ. The relative intensity of p_{22} in the single spectrum which is consistent with the previous value as well and thus there is no need to worry about p_{22}.

4.4.2. Gate around the 2613.8(11) keV γ peak

The gate around the 2613.8(11) keV γ peak is constructed as outlined for the 1633.602(15) keV γ gate and visualised in figure A.8. The gated coincidence spectra are also generated similarly to the spectra for the 1633.602(15) keV gate and below is a list of the peaks expected to be found in coincidence with a 2613.8(11) keV γ.

p_4; 885(14) keV: p_4 is considered in the U3 detector. There are few counts; eight in the spectrum and eight in the background to be specific. With these few counts an upper limit on the content of p_4 is constructed. For this upper limit estimation the Garwood 95% confidence interval from [2] is used. A low limit for the eight background counts is estimated with the Garwood 68% interval and subtracting the low limit on the background from the upper limit of the spectrum count gives an upper limit of 9.2 counts. With this primitive and intuitive method a conservative upper limit on the relative content of the coincidence peak is determined to be

$$\frac{N_{p\gamma}}{N_p\,\varepsilon_\gamma} = 0.078(17) \ . \tag{4.22}$$

According to [13] p_4 should be the most intense peak in the low-energy triplet but this shows that either p_4 is substantially less intense than previously determined or it is plotted in falsely in the decay scheme or the 4^+ level in ^{20}Ne has another intense decay mode that circumvents the 2613.8(11) keV γ decay.

p_7; 1386(14) keV: The number of counts associated with p_7 in the 2613.8(11) keV γ gate is very scarce. To be conservative in the estimate of the content the U4 detector is used for the analysis as it shows the most counts. With the same intuitive method as for p_4 in this γ gate an upper limit on the content is determined using the Garwood upper limit [2]. This results in an upper limit on the relative content of

$$\frac{N_{p\gamma}}{N_p\,\varepsilon_\gamma} = 0.31(10) \ . \tag{4.23}$$

This is considerably less than anticipated and thus p_7 can only be coincident with the 1633.602(15) keV γ. This means that p_7 seemingly goes from a lower level in ^{21}Na and directly to the first excited state in ^{20}Ne.

p_9; 1546(12) keV: The most counts belonging to p_9 in coincidence with a 2613.8(11) keV γ is found in the U3 detector, but the background in U3 has an equal content. The construction of an upper limit on the coincidence peak content is carried out like for p_4 in

the 2613.8(11) keV γ gate. This reveals an upper limit on the relative peak content of

$$\frac{N_{p\gamma}}{N_p\,\varepsilon_\gamma} = 0.71(19)\ ,\tag{4.24}$$

and as this value is consistent with 1 within 1.5σ, the possibility of a coincidence is confirmed.

p_{14}; 2181(2) keV: The U3 detector shows p_{14} in coincidence with a 2613.8(11) keV γ as expected. The content of this coincidence peak relative to the total content of the combines p_{13}-p_{14} peak in the single spectrum is

$$\frac{N_{p\gamma}}{N_p\,\varepsilon_\gamma} = 0.9(3)\ .\tag{4.25}$$

This shows that p_{14} is at least as intense as p_{13} which contradicts the previous result.

4.4.3.   GATE AROUND THE 3332.54(20) keV γ PEAK

The gate around the 3332.54(20) keV γ peak is visualised in figure A.9 and the results of the coincidence analysis with this gate are listed below.

p_2; 862(12) keV: d Components from the low-energy triplet are measured in the U4 detector. The content of the coincidence peak relative to the single spectrum is

$$\frac{N_{p\gamma}}{N_p\,\varepsilon_\gamma} = 0.15(5)\ .\tag{4.26}$$

Including the small correction for the γ decay branching ratio from table 4.1 this number still correspond to a fraction of approximately 15% of the triplet peak being in coincidence with a 3332.54(20) keV γ. This is presumably mostly p_2 but also p_3 can contribute through the less intense γ decay branch $3^- \rightarrow 2^- \rightarrow 2^+$ (see table 4.1). Assuming all the 3332.54(20) keV photons are coincident with p_2 this corresponds to a relative intensity of p_2 which in consistent with the previously determined value.

p_8; 1502.7(19) keV: Counting the hits associated with p_8 in the U3 detector gives a measure of the relative content of

$$\frac{N_{p\gamma}}{N_p\,\varepsilon_\gamma} = 0.9(3)\ ,\tag{4.27}$$

which fits the expectations nicely.

4.4.4.   GATE AROUND THE 3987.3(17) keV γ PEAK

The gate constructed around the 3987.3(17) keV γ peak is illustrated in figure A.10. Only one proton peak is expected to be in coincidence with a 3987.3(17) keV γ.

p_3; 879(3) keV: Generally, there are very few counts in the coincidence spectra with the 3987.3(17) keV γ peak. In the energy range that can be associated with the low-energy triplet, U2 shows the most counts compared to U3 and U4; three counts with no

background. Using the Garwood upper limit from [2], this gives an upper limit on the coincidence spectrum content relative to the content of the low-energy triplet peak in the single spectrum of

$$\frac{N_{p\gamma}}{N_p \, \varepsilon_\gamma} = 0.065(14) \ . \tag{4.28}$$

Here it is important to remember that the $3987.3(17)\,\mathrm{keV}$ γ decay does not constitute 100% of the γ decay from the 3^- level. Correcting for the γ decay branching ratio, the upper limit on the fraction of the low-energy triplet that belongs to p_3 is $0.075(16)$. Though it does not look like much this actually corresponds to a relative intensity which is larger than the previously assigned relative intensity and it seems safe to say that the coincidence between p_3 and the $3987.3(17)\,\mathrm{keV}$ γ is possible.

4.4.5. β-delayed proton branches to the ground state in ^{20}Ne

The peaks corresponding to proton transitions to the ground state in ^{20}Ne should not be visible in the coincidence spectra. The analysis reveals that neither of the peaks can be associated with content in the coincidence spectra that would be consistent with a transition to an excited state in ^{20}Ne. Nevertheless, the most intense peaks to the ground state have a certain probability of arriving in random coincidence with a γ and thus faintly appear in the coincidence spectra. This is the case for especially p_{10} and p_{11} but should not cause apprehension. Possibly, p_{16} appears a bit in the coincidence spectrum as well and this might cause some of the overestimation of the p_{15} content relation though the impact will be small.

The determination of the relative intensities of the peaks in the single spectra are approximately as good as can be expected with the simple Gaussian fits. An R-matrix analysis would have been preferable but that is beyond the scope of this project. Some caution must be taken when estimating the content of the peaks p_{16} and p_{18} as they overlap and interfere. Even a seemingly reasonable division of the peaks is not necessarily correct and thus no harsh conclusions should be made from the relative intensities of p_{16} or p_{18}.

4.5. Summarizing the results; decay scheme and relative intensities

The previous section 4.4 presented a lot of results and considerations and these are summarized here in two tables showing the decay scheme and the relative intensities respectively.

Decay scheme

The coincidence analysis has confirmed the placement of most at the peaks in the decay scheme. These confirmed peaks are listed in upright font with no additional marks in their respective places in table 4.4. For the peaks p_3 and p_9 only the construction of an upper limit has been possible for their coincidence with a $3987.3(17)\,\mathrm{keV}$ and a $2613.8(11)\,\mathrm{keV}$ γ respectively. An upper limit is not solid confirmation of the coincidence but an indication of a clear possibility that the coincidence is true. Moreover, for the p_9 there exists no suitable

$E_{^{21}Na}$ [keV]	^{20}Ne level [MeV, J^{π}]				
	0.0, 0^+	1.63, 2^+	4.25, 4^+	4.97, 2^-	5.62, 3^-
3544.3 (4)	p5				
4294.3 (6)	p10	x			
4467.9 (7)	p11	p1			
5020 (9)	p15	p4.2?			
5380 (9)	x	p6			
5884 (20)	p16	x			
6165 (30)	x	p12			
6341 (20)	x	p13			
6468 (20)	p18	x			
7609 (15)	p23	p17	(p4)	x	
8135 (15)	x	x	~~p7~~	x	x
8303 (13)	p24	p19	$p9$	p2	x
8397 (15)	p25	p20	x	x	x
8827 (15)	p26	p21	x	x	x
8976 (2), $T = \frac{3}{2}$	p27	p22	p14	p8	$p3$
9725 (25)	p28	x	x	x	x

Table 4.4: The peaks from [13] are placed in their respective places. Upright writing with no additional marks signifies a confirmation of the placement. Peak name in italic means that the peak might possibly be placed here based on an upper limit on the content. $(p4)$ in braces means that there might still be some part of $p4$ to this level in ^{20}Ne but definitely not the same amount as previously assigned. The crossing out of $p7$ signifies that the present coincidence analysis shows evidence that $p7$ can not be placed here. The question mark next to the new peak $p_{4.2}$ means that this peak is proposed as a result of this analysis. The energies are from [17].

energy state in ^{21}Na that could decay to the first excited state in ^{20}Ne by emission of a proton with energy corresponding to the $p9$ peak. Thus the previous placement of $p9$ is deemed trustworthy.

With $p3$ it is a slightly more complicated matter as $p3$ is part of the low-energy triplet together with $p2$ and $p4$. The upper limit on the content of $p3$ in the 3987.3(17) keV γ coincidence spectrum allows $p3$ to be consistent with the previous placement in the decay scheme. As the content measure is based on an upper limit the result also allows for $p3$ *not* to be coincident with a 3987.3(17) keV γ. However, the coincidence between $p3$ and a 3987.3(17) keV γ can not be dismissed based on this analysis and thus $p3$ keeps its place in the decay scheme.

A component of the low-energy triplet is also coincident with a 3332.54(20) keV γ and this component is called $p2$. This leaves the presumably largest component in the low-energy triplet, $p4$, which previously was placed in coincidence with a 2613.8(11) keV γ. The yield of low-energy counts in coincidence with a 2613.8(11) keV γ is numerous times too small to account for the remaining content of the low-energy triplet and, moreover, it is an upper limit so possibly there is no coincidence between the low-energy triplet and

a 2613.8(11) keV γ. Hence, I propose a component in the low-energy triplet, $p_{4.2}$, which goes directly to the first excited 2^+ state in ^{20}Ne. This component would connect the 5020(9) keV level in ^{21}Na with the 1633.674(15) keV level in ^{20}Ne. As the 5020(9) keV level in ^{21}Na has $J^\pi = (\frac{3}{2}, \frac{5}{2}, \frac{7}{2})^+$ this is a very possible resonance. The energy of $p_{4.2}$ would then be 955(9) keV which is approximately 80 keV higher than the energy of the other components in the low-energy triplet - which now might be a quartet - but this does not seem like a problem given the broad structure of the low-energy ensemble.

p_7 is problematic. The upper limit of the coincidence between p_7 and a 2613.8(11) keV γ deems p_7 inconsistent with such a coincidence. If, in stead, p_7 goes to the first excited state in ^{20}Ne, the observed energy of p_7 would require the transition to be from the 5457(1) keV level in ^{21}Na. But this level in ^{21}Na has $J^\pi = \frac{1}{2}^+$ and thus can not decay by proton emission to the 2^+ state in ^{20}Ne. The best option for a decaying level in ^{21}Na is then the 5380(9) keV level which also p_6 is connected to. This would imply p_7 being no more than a part of p_6 and this contradicts the seemingly clear division in two peaks we see in the single spectrum. Another possibility is for p_7 to go straight to the ground state in ^{20}Ne. The content of p_7 in coincidence with a 1633.602(15) keV γ is determined as an upper limit and thus this coincidence is not necessarily true. A p_7 transition to the ground state would require a suitable level in ^{21}Na with an energy of approximately 3820 keV. As such a level is not identified with a suitable J^π this interpretation would require a new level in ^{21}Na or a reinterpretation of the spin and parity of an existing level. The lower levels in ^{21}Na are generally well known and thus this is not an apparent solution. Hence the placement of p_7 remains an identified problem with no straight forward solution and p_7 is crossed out in table 4.4 as a consequence of this analysis.

Relative intensities

The calculated intensities are shown in table 4.5. Generally, these new relative intensities should be used with reasonable caution. As mentioned earlier the content of the peaks in the single spectra is determined with fits as the events are too numerous for counting. These fits are obtained with Gaussian functions which is an approximation to the shape of the peaks. As mentioned, a thorough analysis would require R-matrix analysis which is beyond the scope of this project and hence it should be kept in mind that the obtained fits are approximations. This entails an additional systematic uncertainty on the relative contents in 4.5 and a deviation of up to approximately 10% with values from the previous study [13] is not regarded a problem.

A few values still have deviations from the previous values which can not be explained by the simple fitting procedure. The relative intensity of p_1, for example, is completely off. This is ascribed to the U2 detector which has been troublesome in more ways: U2 is very thin and thus picks up a relatively large amount of noise compared to good counts. Moreover, U2 has an uneven thickness and a bad energy resolution so, overall, U2 is not very useful here and results from U2 should not be taken too seriously.

The relative intensity of p_4 has already been described previously in this section as this relative intensity is calculated from the content of the coincidence spectrum. The low relative intensity of p_4 is a result that points to another component in the low-energy

	Relative intensities [%]	
	This study	Previous study [13]
p_1	25.8 (24)	3.91 (45)
p_2	2.35 (82)^a	2.0 (5)
p_3	16.0 (17) $\Big\{$ 1.04 (25)^{ab}	0.28 (3)
p_4	1.25 (30)^{ab}	19.4 (5)
p_5	3.68 (12)	3.34 (6)
p_6	21.26 (42)	20.01 (15)
p_7	2.52 (21)	2.84 (11)
p_8	4.13 (23)	4.66 (9)
p_9	1.34 (26)	2.95 (17)
p_{10}	48.82 (91)	44.05 (24)
p_{11}	100.0 (25)	100.0 (4)
p_{12}	5.18 (18)	4.58 (14)
p_{13}	3.21 (28) $\Big\{$ 0.5 (11)^c	3.79 (55)
p_{14}	2.7 (10)^a	0.73 (20)
p_{15}	16.5 (22)	20.89 (24)
p_{16}	38.3 (23)	34.6 (31)
p_{17}	3.5 (6)	8.0 (15)
p_{18}	27.8 (33)	33.58 (245)
p_{19}	2.08 (33)	1.99 (20)
p_{20}	1.74 (36)	1.94 (19)
p_{21}	7.8 (11)	10.9 (8)
p_{22}	22.5 (17)	24.29 (176)
p_{23}	3.39 (97)	5.63 (75)
p_{24}	1.49 (54)	1.56 (18)
p_{25}	1.52 (34)	1.37 (13)
p_{26}	2.67 (59)	2.86 (29)
p_{27}	7.31 (61)	8.85 (65)
p_{28}	0.06 (2)	0.05 (2)

^{a}Indicidual relative intensity constructed using the content of the coincidence peak.
^{b}This is an upper limit on the relative intensity.
^{c}Calculated as the residual that does not belong to p_{14}.

Table 4.5: Relative proton peak intensities measured in single spectra with respect to p_{11}. The low-energy ensemble and p_{13}-p_{14} were observed as a single peak in the single spectrum.

ensemble which can contribute with the otherwise missing intensity.

The relative intensity of p_{13} and p_{14} is considered in combination and the individual relative intensities are then calculated from the share of the total content attributed to p_{14} by the coincidence spectrum. This changes the ratio between their relative intensities compared to previous results. Now p_{14} has a significantly larger relative intensity whereas the corresponding relative intensity for p_{13} is much lower. Their combined relative intensity is lower than the previously determined value, but even if the present combined relative intensity is actually underestimated and all the remaining intensity is added and attributed to p_{13} the relative intensity of p_{13} will still decrease. This is a new result.

As argued, the results for p_{17} seems off due to insufficient content measured in the single spectrum. p_{17} is located on the slope in a possible interference region and thus the measurement of the content might be influenced. Despite of caution taken when counting the content and adding the background this remains a problem that might need more advanced considerations.

The content measurement on p_{28} is unreliable as the few counts associated with p_{29} are located on a background of comparable size. Hence this value should be handled with a little extra suspicion. However, there is no evidence that the previously determined relative intensity of p_{28} should be wrong.

OUTLOOK

There is still a few challenges left after the conclusion of the analysis described above. The detection of p_1 in the U2 detector is untrustworthy because of the problems with U2. p_1 is very low-energetic and thus often disappears in the background. A future task should be to confirm presence and relative intensity of p_1. Another point for future work is the new $p_{4.2}$ peak. As it is proposed in this analysis, some confirmation from elsewhere would be desirable. This could for instance involve an advanced line shape analysis on spectra from a detector setup with good energy resolution. Also p_7 and p_{17} call for more attention. p_7 currently does not fit in anywhere in the decay scheme based on the coincidence analysis but is clearly an independent peak in the single spectrum so here is challenge for future analysis. During this future analysis it would be interesting to expand the potential of the analysis, especially of the relative intensities, by involving a more advanced fitting routine like the R-matrix analysis. A more advanced fitting procedure is expected to improve the relative intensity analysis considerably and maybe even explain the bewildering shortage of counts associated with p_{17} in the single spectrum.

The coincidence analysis presented here has involved proton spectra for gates on γ energies. The reversed case where γ spectra are constructed with gates on proton energies is also interesting. Maybe then the $3987.3(17)\,\mathrm{keV}$ γ peak will be visible and in any case it will serve as a check and possible consolidation of the results of the coincidence analysis performed here.

In a broader perspective the setup used for the April 2015 experiment shows great potential. It has a larger solid angle coverage than earlier experiments which gives a better efficiency for the same amount of protons which is something we always seek to improve. In addition, the setup includes the γ detectors at the ISOLDE Decay Station which has its obvious advantage in the ability to make the coincidence analysis between particles and γ-rays. Hence, this setup will be utilized for future experiments. One downside to this setup compared to the one used for the November 2011 experiment is its insensitivity to α particles. In the November 2011 a gas telescope was included which provided data for the faint β-delayed particle emission branches involving α particles. In the April 2015 setup there is no detector opposing the U5 detector and maybe a gas telescope would fit nicely there to construct a close to optimal setup for future experiments.
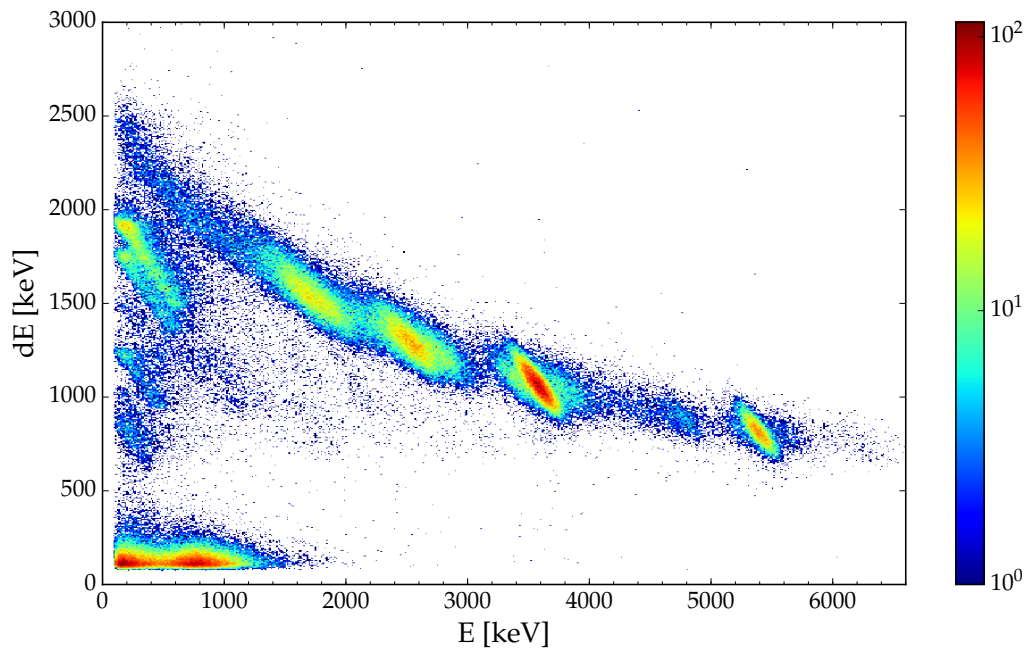
Extra figures

A.1. Related to section 4.3

Figure A.1: The figure shows the dE-E spectrum for the U3-P3 detector telescope. U3 is $60\,\mu$m and P3 is $500\,\mu$m. THis plot shows clear proton peak structure. The two upper peaks close to the axis correspond to the peaks p_{10} and p_{11} which are sufficiently intense to have a certain probability of hitting in coincidence with a β. The figure has 500×500 bins.
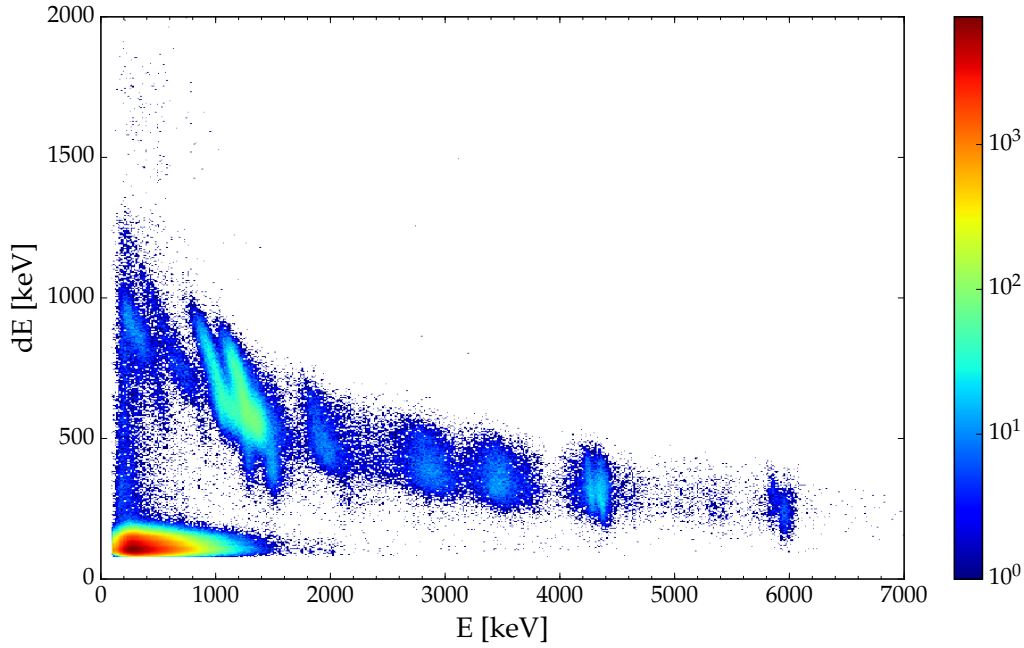
Figure A.2: This figure shows a dE-E spectrum for the U2-U1 detector telescope which consists of a $20\,\mu$m detector in front of a $500\,\mu m$ detector. The figure has $500{\times}500$ bins.
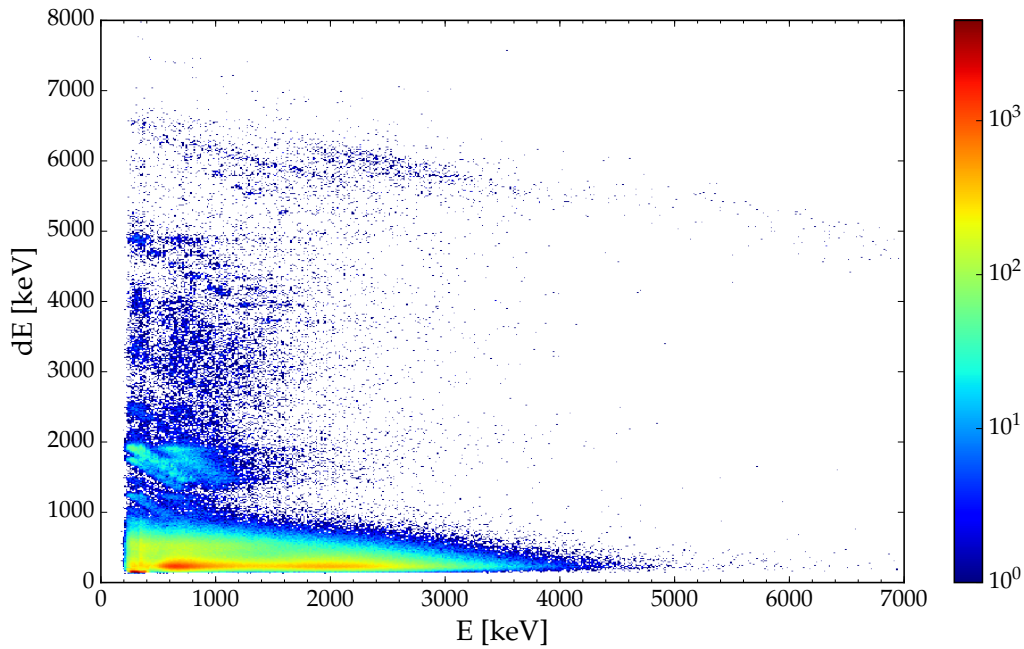
Figure A.3: This figure contains the dE-E spectrum for the U6-P2 telescope with a thick $300\,\mu$m detector in front of a $500\,\mu$m detector. The additional vertical structure in the spectrum might be caused by poor timing in the time alignment.

A.2. RELATED TO SECTION 4.4.1
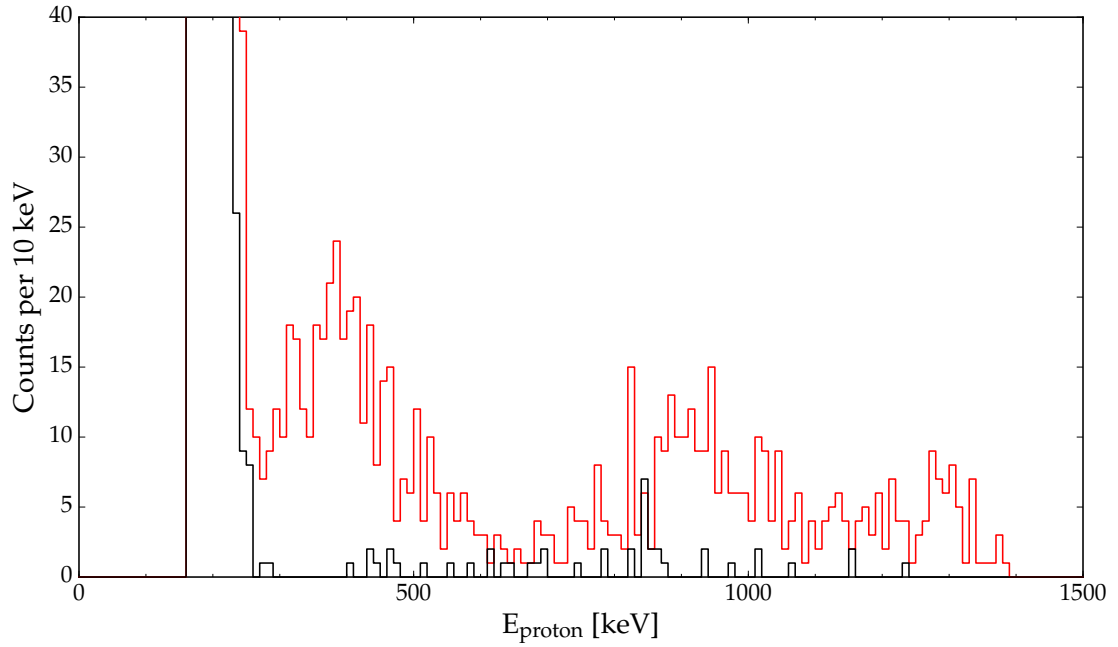
Figure A.4: Coincidence spectrum in the $20\,\mu$m U2 detector with a gate around the $1633.602(15)\,$keV γ peak. The gate is marked in figure 4.8. The red spectrum shows the good events and the black spectrum shows the background. This spectrum has a heavy background content at the lowest energies.
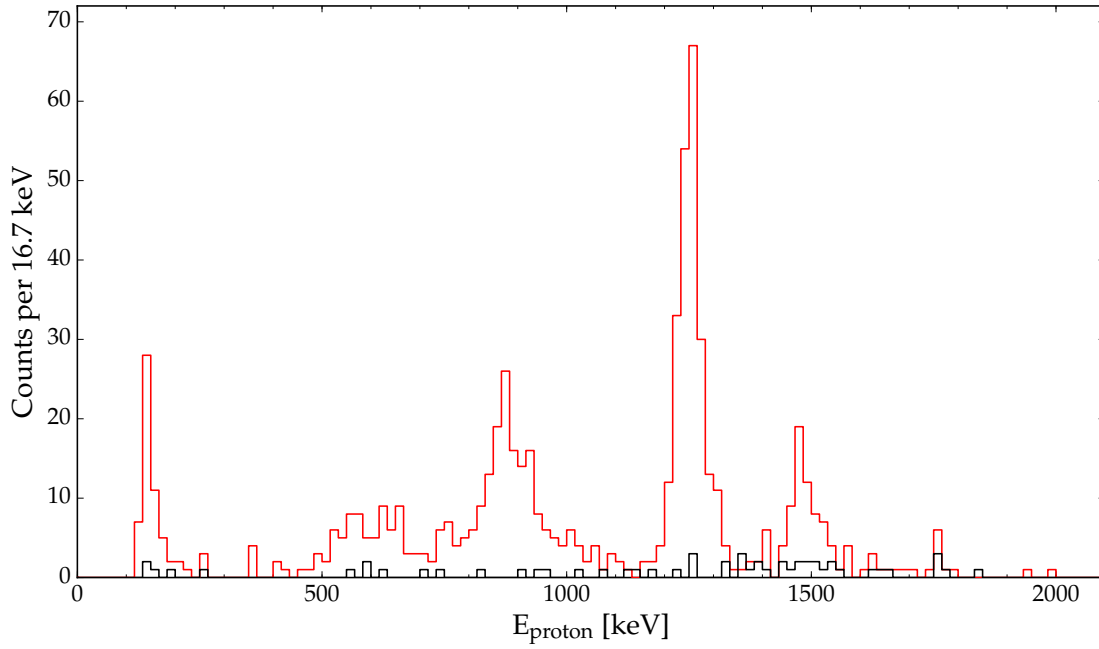
Figure A.5: The 40 μm U4 detector shows this coincidence spectrum for the 1633.602(15) keV γ gate. The prominent peak at approximately 1250 keV is a clear sign of p_6. The red spectrum shows the good events and the black spectrum shows the background. The background is mostly from ^{21}Mg.
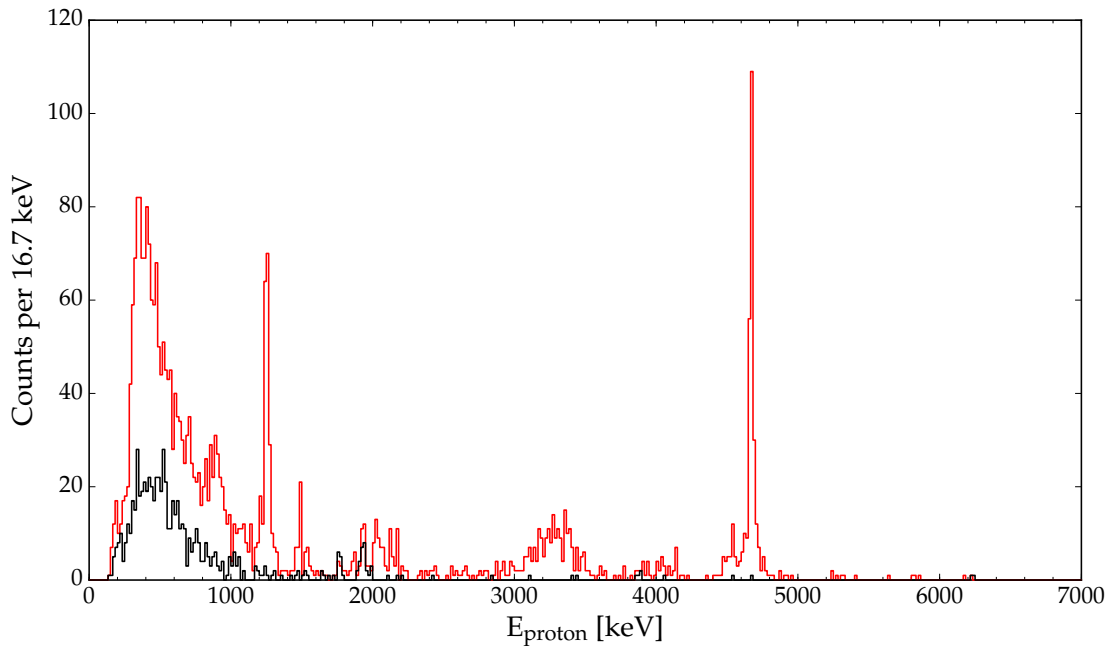
Figure A.6: Coincidence spectrum in the 1000 μm U5 detector for the 1633.602(15) keV γ gate. The red spectrum shows the good events and the black spectrum shows the background. The intense, narrow peak just below 5000 keV is p_{22}.
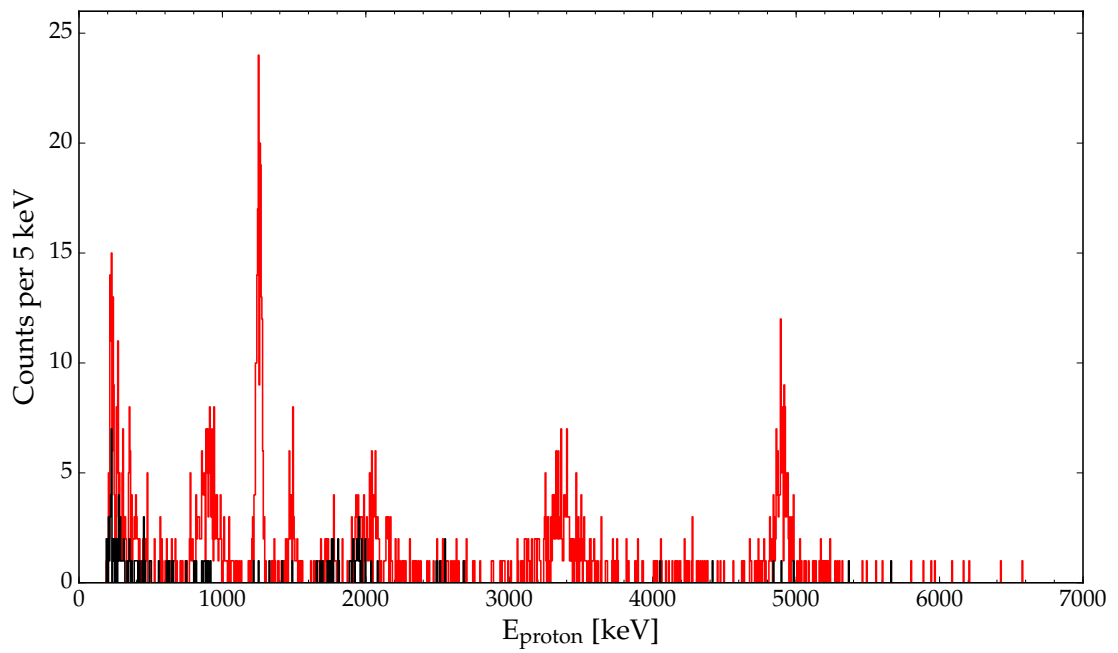
Figure A.7: Less useful coincidence spectrum from the $300\,\mu$m U6 detector with a gate around the $1633.602(15)\,$keV γ peak. The red spectrum shows the good events and the black spectrum shows the background.
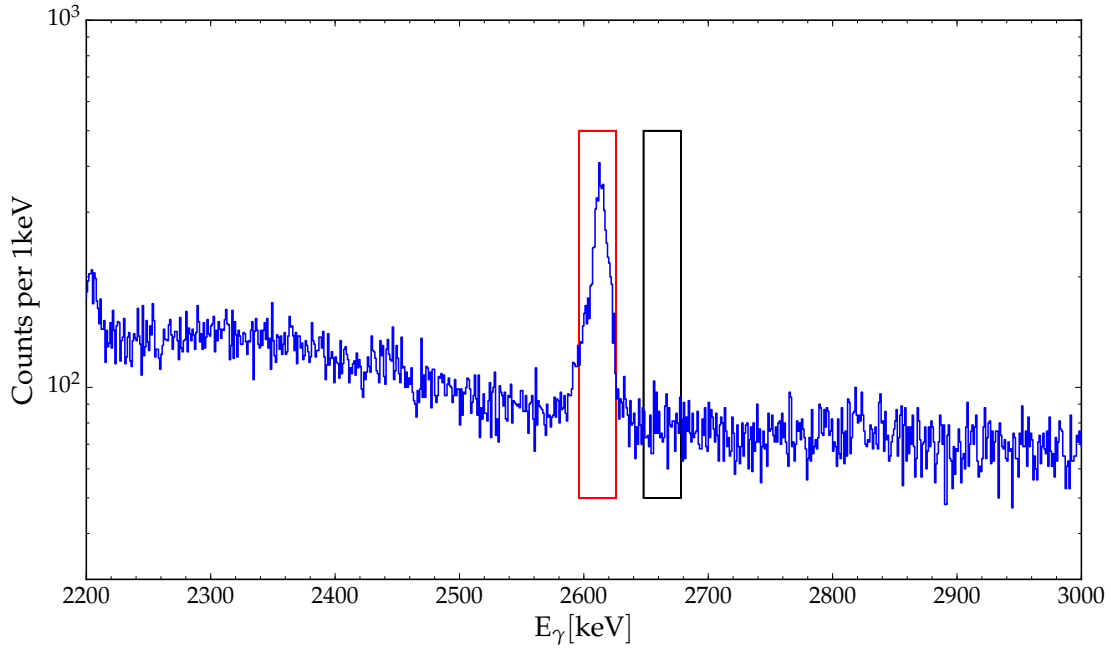
A.3. RELATED TO SECTION 4.4.2

Figure A.8: γ spectrum with the gate on γ energies marked in red on top of the spectrum. This is the 2613.8(11) keV γ gate. The gate energy range is $[2596\,\text{keV} - 2626\,\text{keV}]$ and marked with red. The black box marks the gate $[2648\,\text{keV} - 2678\,\text{keV}]$ used for the background coincidence spectrum.

A.4. RELATED TO SECTION 4.4.3
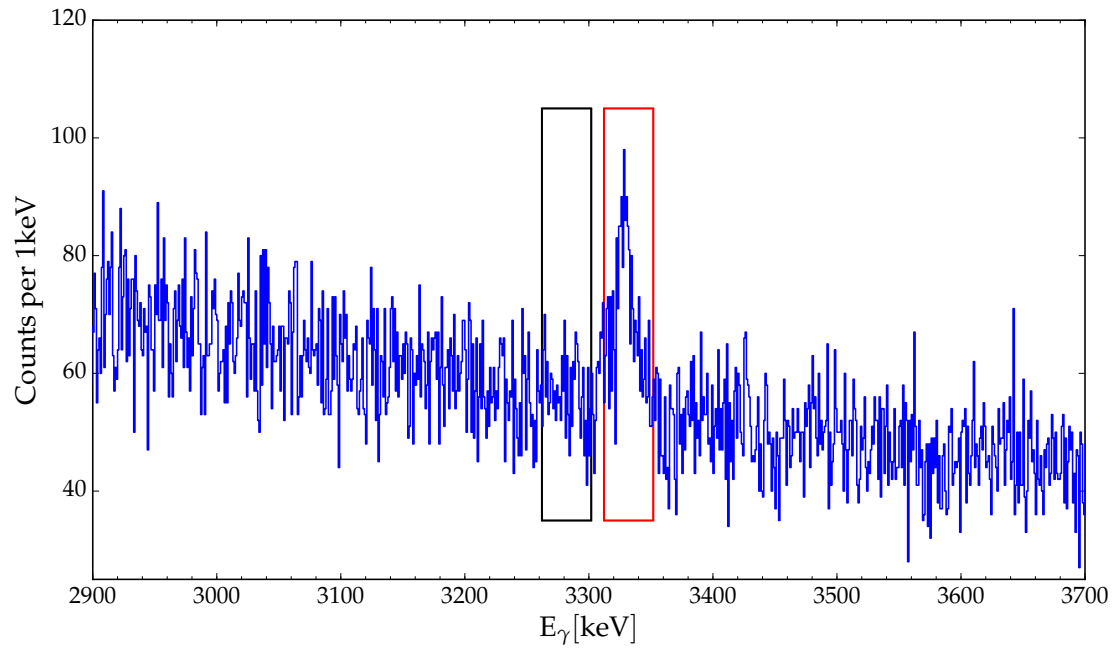
Figure A.9: Illustration of the 3332.54(20) keV γ gate. The gate energy range is $[3312\,\mathrm{keV} - 3352\,\mathrm{keV}]$ and marked with red. The black box marks the gate $[3262\,\mathrm{keV} - 3302\,\mathrm{keV}]$ used for the background coincidence spectrum.

A.5.   RELATED TO SECTION 4.4.4
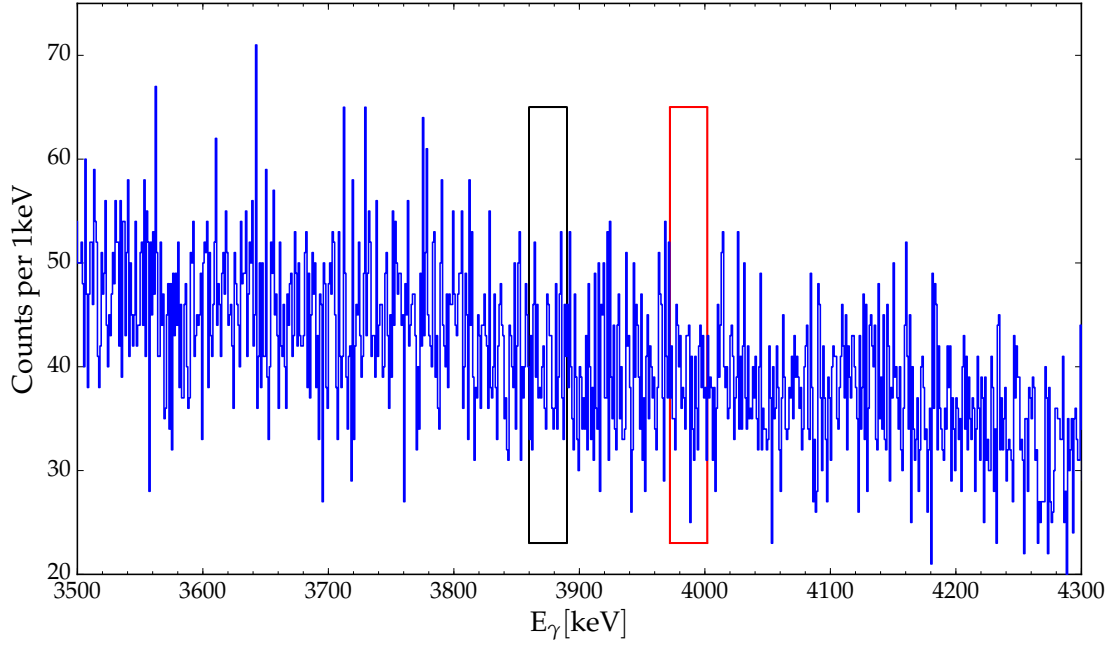
Figure A.10: This shows the range of γ energies that includes the 3987.3(17) keV γ line. A γ gate is constructed at presumably appropriate energies. The red box marks the coincidence gate at $[3972\,\text{keV} - 4002\,\text{keV}]$. The black box marks the gate $[3860\,\text{keV} - 3890\,\text{keV}]$ used for the background coincidence spectrum.

Bibliography

[1] CERN 2014-16. ROOT. `https://root.cern.ch/`. [Online; accessed 20-September-2016].

[2] O. Behnke, K. Kröninger, G. Schott, and T. Schörner-Sadenius. *Data Analysis in High Energy Physics*. WILEY-VCH Verlag GmbH & Co., 2013.

[3] U. C. Bergmann and K. Riisager. New statistical methods for exotic nuclei. *Nuclear Physics A*, 701(1):213 – 216, 2002.

[4] CERN. Accelerator Complex. `http://te-epc-lpc.web.cern.ch/te-epc-lpc/machines/lhc/general.stm`. [Online; accessed 06-November-2016].

[5] CERN. ISOLDE facility. `http://home.cern/about/experiments/isolde`. [Online; accessed 06-November-2016].

[6] K. A. Olive et al. (Particle Data Group). Passage of particles through matter. *Chin. Phys. C*, 38, 010009, 2014 (update 2015). [Online; accessed 18-October-2016].

[7] H. O. U. Fynbo. Beta-delayed particle emission from the dripline nuclei ^{11}Li, ^{31}Ar & ^{9}C. *PhD thesis, Department of Physics and Astronomy, Aarhus University*, 1999.

[8] J. Halkjær. Energy Loss Calculator. `https://eloss.kern.phys.au.dk/`. [Online; accessed 20-September-2016].

[9] P. E. Hodgson, E. Gadioli, and E. Gadioli Erba. *Introductory Nuclear Physics*. Oxford University Press, 1997.

[10] H. B. Jeppesen. Low-energy nuclear reactions with the radioactive isotope ^{9}Li at REX-ISOLDE. *PhD thesis, Department of Physics and Astronomy, Aarhus University*, 2004.

[11] G. T. Koldste. Deciphering drip-line decays - the case of ^{31}Ar. *PhD thesis, Department of Physics and Astronomy, Aarhus University*, 2015.

[12] W. N. Lennard, H. Geissel, K.B. Winterbon, D. Phillips, T.K. Alexander, and J.S. Forster. Nonlinear response of Si detectors for low-Z ions. *Nuclear Instruments and Methods in Physics Research Section A: Accelerators, Spectrometers, Detectors and Associated Equipment*, 248(2):454 – 460, 1986.

[13] M. V. Lund. A search for exotic decay modes on the protondrip-line - the cases of $^{20-21}$Mg. *PhD thesis, Department of Physics and Astronomy, Aarhus University*, 2016.

[14] M. V. Lund et al. Beta-delayed proton emission from ^{21}Mg. *The European Physical Journal A*, 51(9):1–16, 2015.

[15] M. V. Lund et al. (IDS Collaboration). Beta-delayed proton emission from ^{20}Mg. *Eur. Phys. J. A*, 52(10):304, 2016.

[16] M. K. Munk. Qualifying exam paper, Department of Physics and Astronomy, Aarhus University. Unpublished.

[17] National Nuclear Data Center (NNDC). Evaluated Nuclear Structure Data File (ENSDF). `http://www.nndc.bnl.gov/ensdf/`. [Online; accessed 18-October-2016].

[18] D. Schardt and K. Riisager. Beta-neutrino recoil broadening in β-delayed proton emission of ^{32}Ar and ^{33}Ar. *Zeitschrift für Physik A Hadrons and Nuclei*, 345(3):265–271, 1993.

[19] U. I. Uggerhøj. Lecture notes from the course "Particle penetration in matter", Department of Physics and Astronomy, Aarhus University, fall 2014. Unpublished.

[20] J. Ziegler. Stopping Range In Matter (SRIM). `http://www.srim.org/`. [Online; accessed 20-September-2016].